Confocal Microscopy of NV Centers in Nanodiamond and Defects in hBN

Steenbergen, Thomas

Confocal Microscopy of NV Centers in Nanodiamond and Defects in hBN

THESIS

submitted in partial fulfillment of the
requirements for the degree of

MASTER OF SCIENCE
in
PHYSICS

Author :	Thomas Steenbergen
Student ID :	s1683462
Supervisor :	Corné Koks
	Prof. dr. Martin van Exter
Second corrector :	Dr. Bas Hensen

Leiden, The Netherlands, July 10, 2023

Confocal Microscopy of NV Centers in Nanodiamond and Defects in hBN

Thomas Steenbergen

Huygens-Kamerlingh Onnes Laboratory, Leiden University
P.O. Box 9500, 2300 RA Leiden, The Netherlands

July 10, 2023

Abstract

In the quest for finding a room temperature stable single photon source (SPS), defects in hexgonal boron nitride (hBN) have gained more and more attention in the previous years. This thesis studies the single photon emitting properties of defects in a multi-layer hBN flake with a home-build confocal microscopy setup. As a reference system, nitrogen vacancy (NV) centers in nanodiamonds (NDs) are measured first, as there luminescent properties are well documented in literature. In order to improve on previous work in this group, polarization selective elements are included in the optical setup. This inclusion allowed measurements of the absorption and emission dipoles of the SPSs and improved our results by (1) reducing the background and (2) allowing more efficient excitation. We found that defects in hBN showed promising results in terms of single photon purity ($g^2(0)$ =0.09 $\pm$ 0.06) and brightness (35 KHz), outperforming the best single NV center ($g^2(0)$ =0.29 $\pm$ 0.07, brightness: 4 KHz). We also found that the hBN defects showed long term (up to 3000 ns) bunching behaviour, possibly related to the excitation power during measurements. This, together with the measurement of different hBN flakes, constitute interesting topics for future investigation.

Acknowledgments

First and foremost, I would like to thank Corné Koks for being my daily supervisor, helping me a lot in the lab and with the analysis of the results. The useful and insightful discussions with him helped propel this project forward.

Secondly, I want to thank Martin van Exter for the monthly discussions and giving direction to the project, especially in the data analysis. His tips and detailed feedback on my writing improved this thesis a lot.

Im also indebted to Moritz Fischer and Nicolas Leitherer-Stenger, who provided the hBN flakes crucial for this project. An insightful discussion of the hBN results improved the analysis provided in this thesis greatly.

Finally, I would like to thank Bas Hensen for being my second corrector and for a helpful discussion of the first obtained results.

Contents

Chapter 1

Introduction

In quantum technologies, the generation of single photons as carriers of quantum information is crucial. A variety of single photon sources (SPSs) has been studied up to this date, under which nitrogen vacancy (NV) centers in diamond [1], carbon nanotubes [2], semiconductor quantum dots [3] and the more recently discovered defects in hexagonal boron nitride (hBN) [4]. A crucial advantage of NV centers and hBN defects is that they operate at room temperatures, which enables rapid characterization and fast research and development cycles [5].

NV centers in diamond have found a broad variety of applications in the last decades. They have been used in quantum teleportation experiments [6], fundamental entanglement experiments over long distances [7] and quantum sensing applications in physics and biology [8]. As SPS however, NV centers are limited by their relative low brightness (highest reported: 2.7 MHz [9]), and outperformed by semiconductor quantum dots, which operate in the GHz regime. In the quest for finding a brighter stable room-temperature SPS, defects in hBN have been showing promising results (highest reported 3.7 MHz [10]).

The main goal of this project is to characterize hBN defects in a home-build confocal microscopy setup, as these samples are not very well known up to this date, and need further characterization. As a reference system, NV centers in nanodiamonds are measured because they are well-characterised in literature. By comparing the results of the hBN defects to the NV centers, we can test the characteristics of the hBN defects. The work presented here builds further on previous projects in this group, where colloidal quantum dots and different hBN samples have been measured in the same optical setup. In order to improve on this previous work, polarization selective elements are incorporated in the input and output

ports of the optical setup.

This thesis is structured as follows. In Chapter 2, the required theoretical background on SPSs is provided, accompanied with short descriptions of NV centers and hBN defects. The experimental setup is described in Chapter 3, as well as the methods of the different types of measurements. Chapters 4 and 5 present the results of the NV centers in nanodiamonds and hBN defects, respectively. In Chapter 6, the results of the previous two chapters are compared, conclusions are drawn, and a brief outlook is given.

Chapter 2

Theory for single photon sources

2.1 Characterization of single photon sources

Single photon sources (SPSs) have the following set of properties which characterize their performance in a non-resonantly driven excitation laser field:

1. *Brightness*. The maximum number of photons the SPS emits.
2. *Saturation power*. The excitation laser power where the photoluminescent intensity is half the brightness.
3. *Purity*. A measure of how pure the stream of photons is coming from the SPSs. Often limited by background photons.
4. *Excited state lifetime*. The time between the absorption of a pump photon and emittance of a single photon.
5. *Blinking*. The exhibtion of ”on” and ”off” states of the emitter over different time scales.
6. *Bleaching*. The irreversible process of decline in photoluminescent intensity over time due to photochemical effects.
7. *Absorption and emission diople* The angular dependence of the polarization of the excitation laser and the polarization of the single photons, respectively.

In this section, the above properties are described in greater detail and the methods performed in this thesis to measure these properties are described. Where saturation measurements are used to obtain information of

the brightness and saturation power, the measurement of a second order correlation function provides information on the purity and excited state lifetime. Blinking and bleaching are characterized by measuring the intensity of the emitted light over time. The absorption and emission dipoles can be extracted by varying the polarization of the excitation laser and by measuring the polarization of emitted photons, respectively.

Saturation curves

Saturation curves are photoluminescence intensity measurements of a SPS as function of the power of the excitation laser. If the laser power is increased, the photoluminescent intensity is increased, as there is a higher chance per unit time for the system to be excited and to emit a photon again. This increase slows down until the luminescence count rate approaches the saturation count rate. The relation between the excitation laser power P and the measured count rate N_{count} is given by:

$$N_{count} = \frac{N_{sat}}{1 + \frac{P_{sat}}{P}} + mP \tag{2.1}$$

where N_{sat} is the saturation count rate (or brightness), P_{sat} the saturation power and m the power dependent background slope. A plot of saturation curves for different values for m is shown in figure 2.1. Here we see that the count rate saturates more clearly in the low background regime, where in the high background case, a more distinct linear increase is visible for high P.

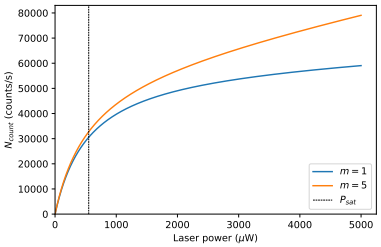

Figure 2.1: *Typical saturation curves for $m = 1$ (blue) and $m = 5$ (orange). The saturation power has typical value 550 μW and the saturation count rate is set at 60 kcounts/s.*

The second order correlation function

In order to understand the dynamics of single photon emission and to have conclusive proof that single photons are created, a normalized second order correlation function ($g^2(\tau)$) needs to be obtained from a Hanbury-Brown-Twiss measurement. This function is a characterization of the fluctuation of light, providing insight in the quantum nature of its source, and is defined as:

$$g^2(\tau) = \frac{\langle I(t)I(t+\tau)\rangle}{\langle I(t)\rangle^2} \tag{2.2}$$

where $I(t)$ ($I(t+\tau)$) is the intensity of the light at t ($t+\tau$) and $\langle\rangle$ denotes the time average. $g^2(\tau)$ describes thus the relation between intensities measured at time t and time $t+\tau$. In terms of single photon sources, $g^2(\tau)$ is the normalized (to a Poissonian source) probability that we detect a photon at time $t+\tau$, given that we measured a photon at time t. Since the photon source has a non-zero excited state lifetime τ_1, the emitter is dark for this lifetime, and will therefore emit no successive photons with temporal separations smaller than τ_1. Thus, if a photon is detected at t, we expect that for $\tau < \tau_1$, $g^2(\tau) = 0$. This is visible as a dip in $g^2(0)$ and is denoted as *antibunching*, proving the quantum nature of the light source. For longer timescales we expect, depending on the excitation power, to observe peaks ($g^2(\tau) > 1$) in the second order correlation function. These peaks are a result of a dark metastable state, which increases the correlation for values of τ that are comparable to the lifetime of this state. This behaviour is denoted as *bunching*. If $g^2(\tau) = 1$, the correlation between photons separated in time by τ is purely Poissonian.

In order to quantify both the bunching and antibunching behaviour of a three level system, we need the parameters describing the transitions between these three levels, which are shown in the figure below for a NV center:

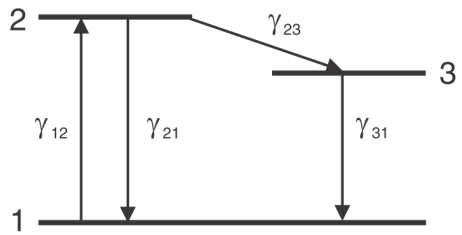

Figure 2.2: *Three level system of an NV center. Reprinted from Novotny and Hecht [11].*

In this figure, levels 1 and 2 are bright triplet states and level 3 is a dark singlet state. The transition rates between the states are denoted by γ [s^{-1}]. γ_{21} is connected to the lifetime of the excited state, γ_{12} to the excitation power (laser power in experiments), and rates γ_{23} and γ_{31} describe the dynamics of the intersystem crossing to the singlet state. With these four parameters, we can write the autocorrelation function as [11]:

$$g^2(\tau) = 1 - \left(1 + \frac{A_2}{A_3}\right) e^{s_1 \tau} + \frac{A_2}{A_3} e^{s_2 \tau} \tag{2.3}$$

where [11]

$$\begin{aligned} s_1 &\simeq -(\gamma_{12} + \gamma_{21}) \\ s_2 &\simeq -(\gamma_{31} + \frac{\gamma_{12}\gamma_{23}}{\gamma_{12} + \gamma_{21}}) \\ \frac{A_2}{A_3} &\simeq \frac{\gamma_{12}\gamma_{23}}{\gamma_{31}(\gamma_{12} + \gamma_{21})} \end{aligned} \tag{2.4}$$

Here, s_1^{-1} and s_2^{-1} are the timescales of the antibunching and bunching, respectively. The theoretical autocorrelation functions for three different excitation powers (γ_{12}) are shown in figure 2.3. Here we observe the following two effects, as the laser power (γ_{12}) is increased:

1. The antibunching timescale is decreased.

2. The bunching amplitude, given by ratio $\frac{A_2}{A_3}$ in equation 2.4, is increased.

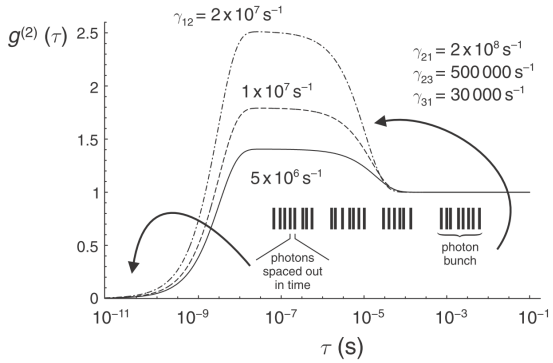

Figure 2.3: *Three level system of an NV center. Reprinted from Novotny and Hecht [11].*

The value of the autocorellation function at zero time delay, $g^2(0)$, provides information on the number of emitters under focus:

$$g^2(0) = 1 - \frac{1}{N} \tag{2.5}$$

where N is the estimated number of emitters. The measurement of $g^2(\tau)$ can thus provide an indication of the number of SPSs, and for $g^2(\tau) < 0.5$, we have a true SPS.

2.2 NV centers in nanodiamonds

NV centers in diamond consist of a substitutional nitrogen atom and a nearest neighbour vacancy of a carbon atom in the diamond lattice structure, as shown in figure 2.4. These centers can be artificially created in nitrogen-rich diamonds by electron-irridiation, which removes carbon atoms at some positions.

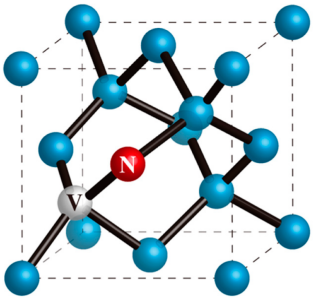

Figure 2.4: *Diamond structure of an NV center, where the blue atoms represent carbon, N the nitrogen atom and V the vacancy. Reprinted from [12].*

This NV center has effectively one unbound electron and can trap an additional electron from its surroundings (nitrogen impurities), turning it into the negatively charged NV^- center. If there is no additional electron trapped, we have the neutral NV^0 center. The energy levels of the NV^- centers are split in triplet ground and excited states and the metastable singlet state, which non-radiatively decays to the triplet ground state. The triplet ground and excited states are split in zero magnetic field due to dipole-dipole interactions. A level diagram of the NV^- center is shown in figure 2.5.

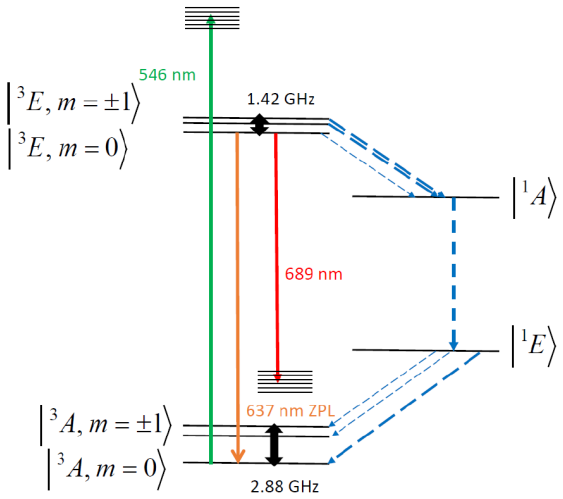

Figure 2.5: *Level diagram of the NV^- center. The triplet ground and excited states are indicated by ^3A and ^3E respectively, while the ground and excited singlet singlet states are indicated by ^1A and ^1E respectively. Reprinted from Michel Orrit's syllabus of the Single Molecule Optics course at Leiden University.*

NV centers are often driven non-resonantly by green laser light, which excites the system to the phonon wing of the triplet excited state. After losing a portion of the energy to phonons, the system decays radiatively to the phonon wing of the ground triplet state or to the ground triplet state itself. The latter transition is called the zero phonon line (ZPL), which emits light with a wavelength of 637 nm and is visible in room-temperature experiments, as shown in figure 2.6.

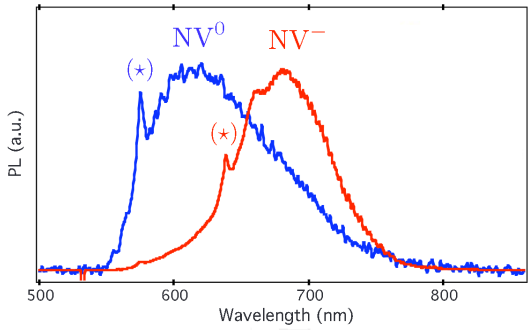

Figure 2.6: *Fluorescence spectra of NV^- (blue) and NV^0 (red) centers in nanodiamonds, where the ZPLs are indicated by the * symbols. Reprinted from [13].*

The triplet ground and excited states are split in the spin $m = 0$ and the nearly degenerate $m = \pm 1$ levels. The ground state splitting is given by

2.88 GHz, while the excited state splitting is 1.42 GHz. The spin $m = \pm 1$ sublevels of the excited state have a higher chance of decaying via the singlet state, and thus not radiating a photon. Fortunately, if the system is excited optically, the $m = \pm 1$ levels become mostly depopulated and the decay occurs via radiative channels. If a magnetic field is applied however, the $m = \pm 1$ levels become more populated and the non-radiative decay via the singlet state is stimulated. Hence, by applying a microwave field, the fluorescence intensity shows a dip at 2.88 GHz. These types of measurements are referred to as optically detected magnetic resonance (ODMR). This magnetic interaction can therefore be used to flip the spin state of an NV center, which can optically by read-out. Also, due to hyperfine splitting, the spin state of the NV can be stored in a nearby C13 atom, effectively functioning as a memory qubit. So due to their relatively bright emission, stable spectra, tunable spin and the possibility of storing the qubit's information in nearby nuclear spins, NV centers are suitable constituents of quantum information systems.

2.3 Defects in hBN flakes

Defects in hexagonal Boron Nitride (hBN) have gained more attention in the previous years as being a SPS candidate. hBN has a honycomb lattice structure similar to graphene with reported bandgaps between 3.6 and 7.1 eV [4]. hBN comes in the following forms: (1) single layer, (2) multilayer (often in flakes) and (3) bulk. Defects in the crystal structure have been shown to exhibit ultra bright linearly polarized sources of light with a high single photon purity at room temperature, making them ideal candidates for SPSs in quantum systems and sensing applications. The precise photoluminescent properties and their connected physical mechanisms are not very well known today and need further investigation. As fabrication procedures influence these properties, large variations have been reported. For example, for the ZPL wavelength, values have been found ranging from the near infrared to the ultraviolet [14].

In multilayer flakes, two groups of defects can be differentiated by the shape and intensity of their ZPL and PSBs. Measured spectra of the groups are shown in figure 2.7(a). The microscopic origin of the two groups is studied in [15] using density functional theory, where defect $V_N C_B$ is proposed for group I and V_B^- for group II. The corresponding lattice structures are shown in figure 2.7(b). The calculated spectra of the defects are shown in green and blue, respectively, in figure 2.7(a).

Version of July 10, 2023– Created July 10, 2023 - 11:45

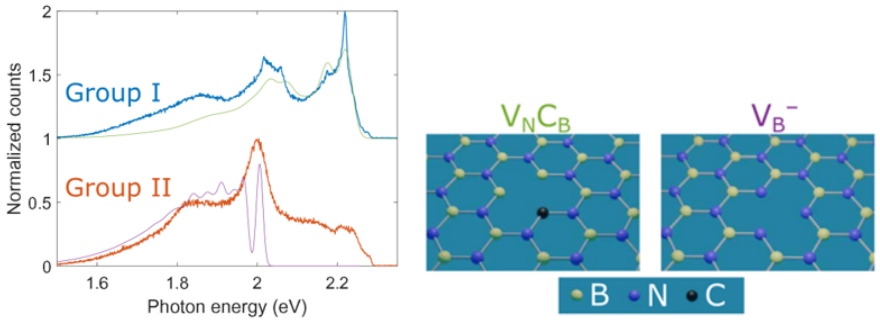

(a) (b)

Figure 2.7: *Fluorescence spectra of NV^- (blue) and NV^0 (red) centers in nanodiamonds, where the ZPL's are indicated by the * symbols. Reprinted from [15].*

In this project, multi-layer hBN flakes are measured. These samples are produced in a three step fabrication process, illustrated in figure 2.8. The first step is exfoliation using a scotch tape technique. The second step is to create defects on the flake, which is done by irradiation with oxygen atoms. The final step is anneealing the samples in nitrogen at 850°.

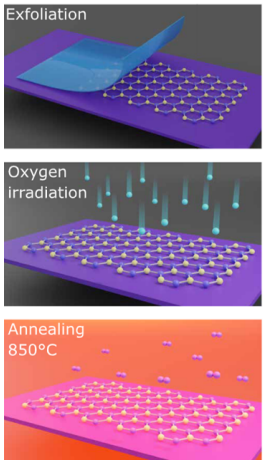

Figure 2.8: *Fabrication steps of hBN flakes with defects. Reprinted from [15].*

Chapter 3

Confocal Microscopy setup

3.1 Setup

The optical setup is shown in figure 3.1, where the abbreviations correspond to the optical elements in table 3.1 First, the non-polarization selective setup is discussed, after which the adjustment to obtain the polarization selective setup are described. The additional elements are indicated in orange in the sketch of the optical setup.

The light from a 532 nm free space laser is coupled with an objective (O) to an angled single-mode optical fiber (SMF 1) on one side of the table and is coupled back to free space on the other side of the table. In order to control the laser power, a variable attenuator (Att) is included, simultaneously functioning as a linear polarizer. The light then passes a 532 $\pm$ 10 nm bandpass filter (SF1), to clean up spectral deviations from the SMF. The green light is reflected by a dichroic mirror (DM) with cut-off wavelength $\lambda_{co} = 520$ nm, which reflects light below λ_{co} and transmits above λ_{co}. As this wavelength is below the center laser frequency, the angle with the dichroic is slightly smaller than 45°, such that the effective cut-off frequency is 540 nm. Using mirrors (M), the excitation light is guided to an apochromatic 100x/0.90 NA objective (FO), focusing the excitation light on the sample. The sample is placed on a piece of glass (NV centers) or on a mirror (hBN flakes), which in turn is placed on a piezoelectric XYZ-stage. The light from the sample is collected by the objective and is transmitted by the dichroic mirror. Then, it passes 2 spectral filters, the first being a 550 nm longpass filter to remove remaining pump light (SF 2), while the second is a 593 nm longpass filter (SF 3), which additionally partly filters out the luminescence of NV^0 centers. Finally, the light is fiber-coupled and can be connected to either the HBT box (indicated by the black rectangle) or a

spectrometer (SM). The HBT box consists of two single photon detectors (SPDs) connected to a start-stop experiment performed with PicoQuant. The inputs of the detectors are connected to a 50:50 in-fiber beamsplitter (FBS). As negative delay times are needed in the start-stop experiment, one of the arms consists of a 10 meter long fiber, inducing a 47 ns time delay. An additionial 100 ns time delay is obtained digitally, gving a total delay of 147 ns. The laser power is measured by the photodiode (PD) collecting the small residual transmission through the DM. The attenuator, the XYZ- stage, the SPDs and the PD are all connected to a PC for control or measurement.

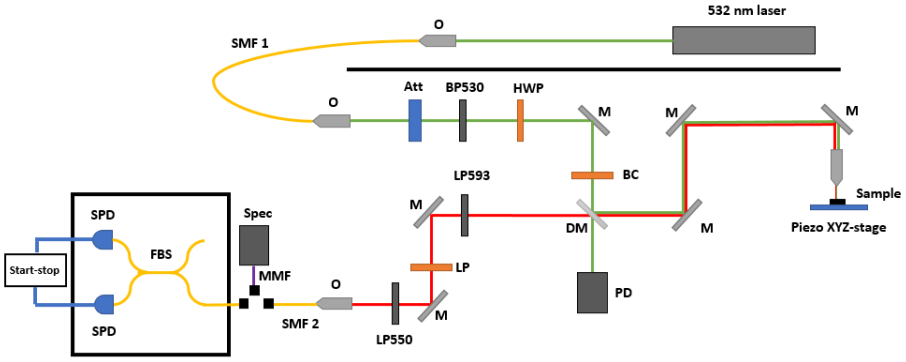

Figure 3.1: *Skecth of the optical setup.*

Abbreviation	Description
532 nm laser	Innolight Prometheus CW narrow bandwidth laser
O	Infinity corrected achromatic objective 20X/0.40 NA from Motic.
SMF 1	Single-mode angled 530 nm optical fiber from Thorlabs
SMF 2	Single-mode 600 nm optical fiber from Thorlabs
MM OF	Multi-mode 600 nm optical fiber from Thorlabs
Att	Liquid crystal optical beam shutter LCC1620(/M) from Thorlabs
BP532	532 ± 10 nm bandpass filter from Thorlabs
HWP	Zero-order $\lambda/2$ plate for 532 nm from Thorlabs
BC	0.2 mm thick birefringent crystal
DM	Dichroic mirror with cutoff frequency of 520 nm from Edmund Optics
FO	Apochromatic objective 100X/0.9 NA WD 2.0 mm from Nikon
Piezo XYZ-stage	NanoCube XYZ Piezo System P-611.3 from PI
LP550	550 nm longpass filter from Thorlabs
POL	Linear polarizer from Glan-Thompson in a rotatable mount
LP593	593 nm longpass filter from Semrock
PD	Home-build photodiode by the electronics department
SPEC	Spectrometer QE65000 from Ocean Optics
SPD	Single-photon-counting module (SPCM) from Excelitas
FBS	In-fiber 630 nm optical beam splitter from Thorlabs

Table 3.1: *List of elements in the confocal microscopy setup.*

3.2 Polarization selective setup

In order to vary the polarization of the excitation laser, a half-wave plate (HWP) is incorporated in the setup in a rotatable mount. To select the polarization of the light emitted by the sample, a linear polarizer (LP) in rotatable mount is placed in the setup. The angles of both optical elements can be adjusted in the Python program. As we found out during calibration measurements, the dichroic mirror complicates the optical setup in two ways (for green light only). The first being that the DM introduces a phase delay between horizontally and vertically polarized light and the second being that the DM has a polarization dependent reflection amplitude. In the following paragraphs, the solutions to these problems are described.

As the dichroic mirror introduces a phase delay $\Delta\phi$ between horizontal (H) and vertical (V) polarizations, the light at the objective becomes elliptically polarized for polarization angles between H and V. In order to correct for this effect, a birefringent crystal (BC) is incorporated in the setup. By varying the tilt of the BC, and thus the distance the light travels in it, a custom phase delay between H and V can be introduced. By setting the phase delay to $-\Delta\phi$, the effect of the dichroic mirror is corrected for and the light is linear at the objective. This tilt was determined by measuring the ellipticity of the light before the objective with a power meter and a linear polarizer. The tilt angle where the ellipticity was minimal for 45 $^\circ$ (H=0°, V=90°) was chosen as the optimal angle.

Besides the introduction of this phase delay, the DM also has a polarization dependent reflection amplitude. In order to correct for this effect, a Python program is written to obtain constant laser powers at the objective for all polarizations. More information on how this is achieved can be found in Appendix A. As the transmitted signal (only for green light) of the dichroic mirror is polarization dependent, the laser power measurement by the PD needs to be calibrated every time a saturation or $g^2(\tau)$ measurement is performed.

3.3 Methods and performance tests

In this section, all measurement methods are described in detail and in some cases, a calibration measurement is provided to asses the performance of the setup.

Version of July 10, 2023– Created July 10, 2023 - 11:45

Spatial scans

In order to find a SPS on a flake or in a nanodiamond, first a large area XY-scan is performed (20x20 μm), where the intensity (in cps) is measured for different positions by moving the piezo XYZ-stage. The intensity is measured by one of the SPDs. After a bright spot (around 5 kcps) is found, a smaller area (1x1 μm) scan is performed with a high resolution (25x25). A typical high resolution XY measurement of a nanodiamond is shown in figure 4.1(a). As the nanodiamonds are only 40 nm in size, which is small compared to the size of focus, we can test how good our focus is. In order to do so, we fit a Gaussian beam waist: w_0 = 0.47 μm. We can compare this beam waist to the Rayleigh range, z_R, which is defined as the HWHM of the peak of the intensity in the Z-scan, which is shown in figure 4.1(b). The beam waist and the Rayleigh range are related by:

$$z_R = \frac{\pi w_0^2}{\lambda} \tag{3.1}$$

where λ is the wavelength of the laser. By measuring the HWHM of the peak, a rough estimate of the Rayleigh range of 1.1 μm is obtained. The expected value for z_R using equation 3.1 is 1.3 μm, which is in rough agreement with measured value for z_R.

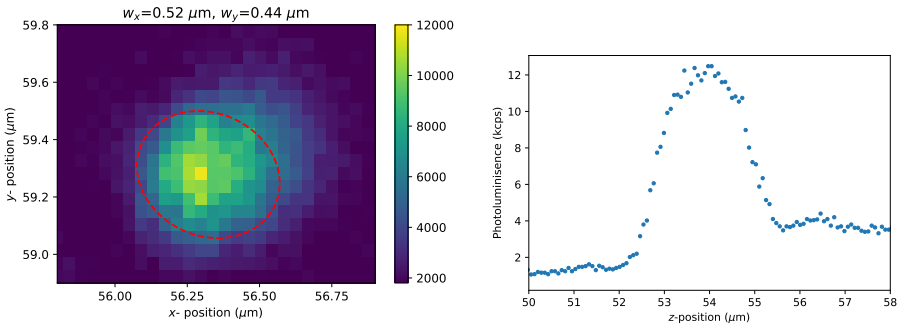

(a) (b)

Figure 3.2: *Spatial scans of two nanodiamonds. The red curve in the xy-scan corresponds to a fit of the Gaussian beam waist. The higher PL intensity from $z = 56$ μm is due to fluorescence of the glass.*

We would expect, however, a much smaller focus size from our objective, as the expected beam waist using $w_0 = \frac{\lambda_0}{\pi \mathrm{NA}}$ is around 190 nm. The origin of this discrepancy is unknown to us, although it has to be noted that in contact with Nikon, this issue has been reported various times before.

Polarization selective measurements

In order to perform a 2D polarization measurement, the HWP and the LP are both rotated over 360° in 15 steps, and for every step the PL intensity is measured by one of the detectors. The final result is a 15x15 diagram of measured intensities.

The polarization selective performance is tested by measuring the polarization visibility for 3 angles before the objective. For this, a linear polarizer is placed at a fixed angle α, before a power meter. By rotating for every α the HWP, we measure a minimum power P_{min} and maximum power P_{max} with a phase difference of $\frac{\pi}{2}$. The visibility is then defined as:

$$V = (1 - \frac{P_{min}}{P_{max}})\text{x}100\% \tag{3.2}$$

which is a direct measure of the linearity of the polarization before the objective. We found $V = 99.9\%$, 99.1% and 99.9% for $\alpha = 0°$, $45°$ and $90°$ respectively, indicating a high linearity of the excitation polarization.

Saturation measurements

A saturation measurement is performed by changing the attenuator voltage and measuring simultaneously the laser power with the PD and the photoluminescence with a SPD. As only one of the SPDs is used in this measurement, the measured intensity is half the total intensity, due to the beamsplitter. Therefore, the values in this thesis for the brightness should all be multiplied by a factor 2.

Spectral measurements

A spectrum is measured by disconnecting SMF 2 from the HBT box and connecting it with a MMF fiber to the spectrometer. As the light from the SPS is usually spectrally spread out (150 nm) and one bin is small (0.4 nm), we need to collect a spectrum over a long period of time (15 minutes) to obtain a high enough signal-to-noise ratio. This long measurement is performed by first performing a dark measurement for 100 s, after which 10 times a spectrum is measured, each taking 100 s. Then, all measurements are added and a Gaussian filter is sometimes used to smoothen the data.

Version of July 10, 2023– Created July 10, 2023 - 11:45

Hanbury-Brown-Twiss and $g^2(\tau)$ normalization

The Hanbury-Brown-Twiss setup consists of two detectors attached to different ends of an in-fiber beam splitter connected to the output fiber of the optical setup. Then a start-stop is measurement is performed: if the start detector measures a photon, τ is set to 0 and the time τ is recorded when a photon is measured by the stop detector. For every 'click' at the stop detector, a 1 is added in time-bin τ.

The raw measurement data from this measurement is thus a histogram of X counts per time bin, with width $w = 0.1$ ns. As the shot noise, SN, is related to the number of counts by $SN \sim \sqrt{X}$, the signal-to-noise ratio can be increased by performing the measurement over long timescales. As the PL intensity of the SPSs in this thesis are usually relatively low (2 kcps), a measurement takes typically 2 hours.

In order to normalize the data to obtain $g^2(\tau)$ from the histogram, two different methods are applied in this thesis:

1. Commonly performed method as described in [16]. Here, the histogram of counts X is normalized to that of a Poissonian source using:

$$g^2(\tau) = \frac{X}{N_1 N_2 w T} \tag{3.3}$$

   where N_1 and N_2 are the count rates at detectors 1 and 2, and T is the total measurement time. The downside of this normalization in the context of our experiments is that $N_{1,2}$ are not constant due to a drift in the XY position of the setup. Since only the count rate at the beginning and at the end are known, this normalization can be erroneous.

2. As the long time scale ($\tau > 800$ ns) behaviour of $g^2(\tau) = 1$ for NV centers is well documented in literature, we can use this to perform a second normalization. First, the average A of the 50 bins between $\tau = 2995$ and 3000 ns is calculated. As $g^2(\tau)$ is expected to be 1 here, normalized is performed by simply using $g^2(\tau) = X/A$. This "dirty" normalization method circumvents the issue of the unknown average count rate and is justified for one NV center by performing both methods and obtaining very similar results. This method is not performed for the hBN defects, however, as the long time scale behaviour is less well-known.

Version of July 10, 2023– Created July 10, 2023 - 11:45

For the first results in this thesis (section 4.1 only), a background correction is performed after normalization. This background is obtained from the saturation measurement, where a residual linear increase (m) with the laser power (P) is determined. The background is then given by $B = Pm$ (in cps). By measuring the intensity S, we can calculate the signal-to-background ratio ρ:

$$\rho = \frac{S}{S + B} \tag{3.4}$$

which we can use to subtract a uniform background using [16]:

$$g^2_{BC}(\tau) = \frac{g^2(\tau) - (1 - \rho^2)}{\rho^2} \tag{3.5}$$

Chapter 4

NV center microscopy

4.1 Non-polarization selective measurements

The xy- scans of two nanodiamonds in the non-polarization selective setup are shown in figures 4.1(a) and (b). The former has a low photoluminescent intensity (7 kcps), while the latter is brighter (30 kcps).

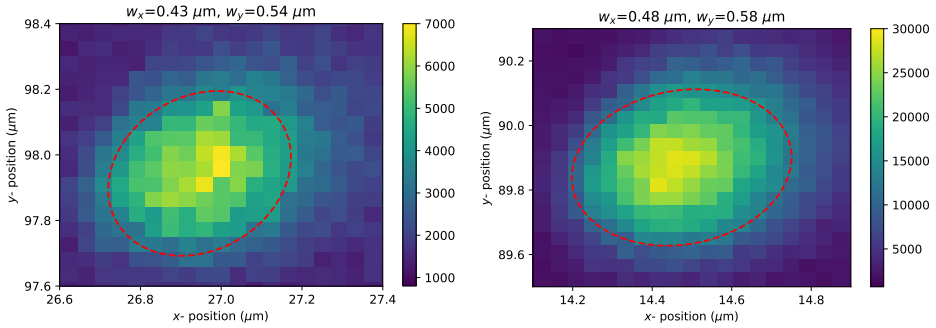

(a) (b)

Figure 4.1: *Spatial scans of two nanodiamonds. The red curves in the xy-scans correspond to a fit of the Gaussian beam waist. Measurement performed at 1000 uW laser power.*

In order to characterize these nanodiamonds further, a saturation measurement is performed of which the data is fitted to equation 2.1, see figure 4.2. From this fit, estimates for the saturation power P_{sat}, the saturation count rate N_{sat} and the background coefficient m are obtained (see inset).

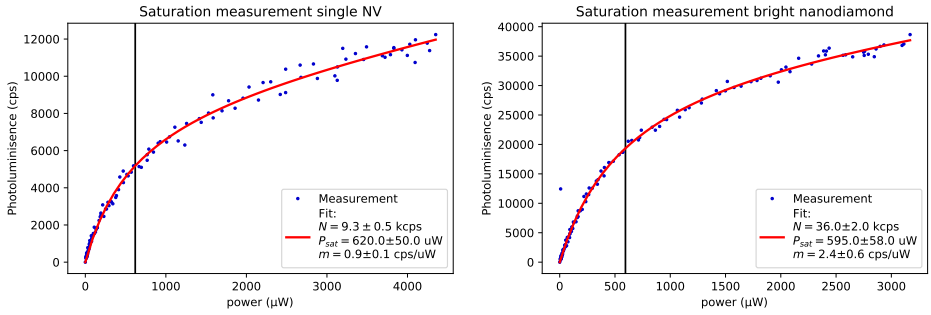

(a) (b)

Figure 4.2: *Saturation curves of the nanodiamonds.*

We observe similar values for the saturation power, while the saturation count rates are significantly different. Also, the background coefficient m is significantly higher for the bright nanodiamond.

The $g^2(\tau)$ measurements are performed with a Hanbury-Brown-Twiss setup as discussed in section 3.2. The results, using normalization method 2 and including background correction, are shown in figure 4.3. For both nanodiamonds, clear dips are visible at zero time delay between detection events, indicating that both are non-classical light sources.

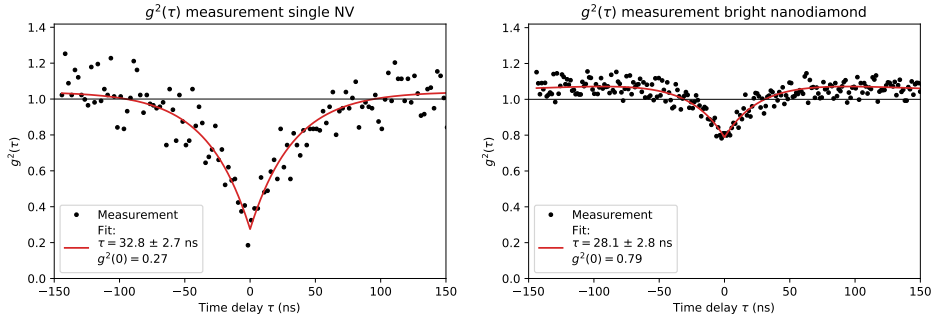

(a) (b)

Figure 4.3: *$g^2(\tau)$ measurement of the single NV nanodiamond (a) and a bright nanodiamond (b). Measurement performed at laser powers 420 μW and 550 μW respectively.*

The measured data is fitted to equation 2.2 to obtain the excited state lifetime τ and the value for $g^2(0)$, as shown in the inset. As the former provides an indication of the number of photoluminescent centers in the nanodiamond, we have found that the first nanodiamond has a single NV

center, as $g^2(0) = 0.27^* < 0.5$ and that the bright nanodiamond probably has 3 or 4 NV centers, since $g^2(0) = 0.79$.

Spectrum, blinking and statistics

For a bright nanodiamond with more than 1 NV center, a spectrum is measured, which is shown in figure 4.4. By comparison with figure 2.6, we can conclude that in this nanodiamond, only NV^- centers are present. The cut-off below 593 nm is due to filter LP593 in figure 3.1.

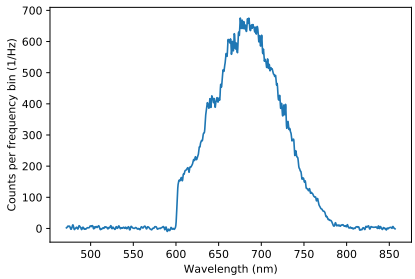

Figure 4.4: *Spectrum of a bright nanodiamond. Spectrum is filtered using a 1D Gaussian filter of order 1.5. The bin size of the frequency axis is 0.37 nm and the laser power was set to 900 μW.*

For a single NV center, blinking was observed over timescales of seconds. A plot of its photoluminescence over time is shown in figure 4.5(a).

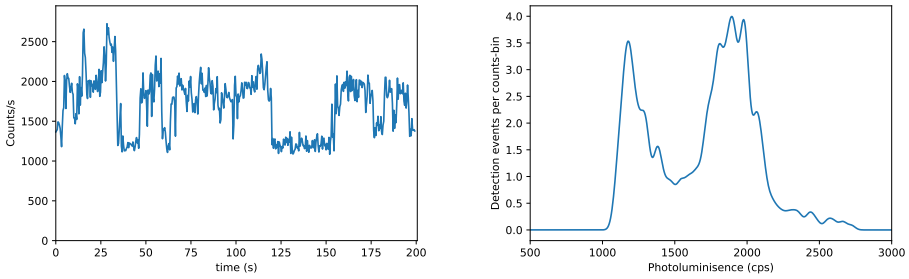

(a) (b)

Figure 4.5: *(a) Time trace measurement of a blinking NV center, performed with 350 μW laser power. (b) Histogram of detection events per number of counts bin, filtered with a Gaussian filter of order 5.*

*Without background correction, $g^2(\tau) = 0.40$

Here we observe that this nanodiamond shows two states of brightness, which can last up to 30 seconds. A histogram of the detection events within a bin size of 5 cps is shown in figure 4.5(b), even more clearly indicating the splitting in two brightness levels. The physical origin of the blinking might be the defect switching between NV^0 and NV^- states, as the results are similar to findings in [17]. Conclusive proof of this claim would constitute a spectrum and a $g^2(\tau) < 0.5$ measurement, of which only the former is unfortunately not present.

For 14 nanodiamonds with varying numbers of defects, all aformenentioned parameters are measured and can be found in table 4.1. Here we briefly discuss some average values. The average saturation power is 660 μW (lowest measured 455 μW, highest 1230 μW) and average antibunching time scale is 32.4 ns (lowest: 20 ns, highest: 75 ns). To gain insight in the average brightness (in terms of N_{sat}) per single NV center, the estimated number of NV centers within a nanodiamond, $\frac{1}{1-g^2(0)}$ is plotted against N_{sat} in figure 4.6. From a linear weighted fit, an average brightness of 11 $\pm$ 1 kcps per NV center is obtained.

Non polarization selective NV center results					
Sample	P_{sat} (μW)	N_{sat} (kcps)	$g_2(0)$	τ (ns)	m (cps/μW)
20230214_2	677 $\pm$44	43$\pm$2	0.85$\pm$0.02	36$\pm$6	3$\pm$0.3
20230216_1	1230 $\pm$ 94	21$\pm$2	0.75$\pm$0.02	35$\pm$5	1.7$\pm$0.2
20230217_1	668$\pm$41	66$\pm$3	0.82$\pm$0.01	29$\pm$2	2.6$\pm$0.6
20230217_2	730$\pm$90	20$\pm$2	0.70$\pm$0.02	23$\pm$2	2.6$\pm$0.4
20230220_1	727$\pm$36	54$\pm$2	0.84$\pm$0.01	30$\pm$2	1.1$\pm$0.4
20230220_3	552$\pm$117	11$\pm$2	0.67$\pm$0.02	76$\pm$20	1.2$\pm$0.3
20230221_5	784$\pm$75	19$\pm$2	0.71$\pm$0.02	31$\pm$3	3.0$\pm$0.3
20230222_1	850$\pm$33	39$\pm$1	0.80$\pm$0.01	23$\pm$2	0.8$\pm$0.2
20230222_2	515$\pm$54	7.1$\pm$0.5	0.47$\pm$0.05	32$\pm$6	1.1$\pm$0.1
20230223_1	470$\pm$25	22$\pm$3	0.64$\pm$0.02	28$\pm$3	1.6$\pm$0.2
20230224_1	618$\pm$70	9.5$\pm$0.7	0.55$\pm$0.04	28$\pm$3	0.4$\pm$0.2
20230227_1	595$\pm$60	36$\pm$3	0.78$\pm$0.01	31$\pm$3	2.6$\pm$0.6
20230227_2	620$\pm$50	9.2$\pm$0.5	0.25$\pm$0.04	33$\pm$3	0.9$\pm$0.1
20230228_1	455$\pm$121	7.2$\pm$1.2	0.22$\pm$0.01	20$\pm$3	2.2$\pm$0.3
20230228_2	499$\pm$38	17$\pm$1	0.55$\pm$0.03	30$\pm$2	0.8$\pm$0.2

Table 4.1: *All measured nanodiamonds in the nonpolarization selective setup.*

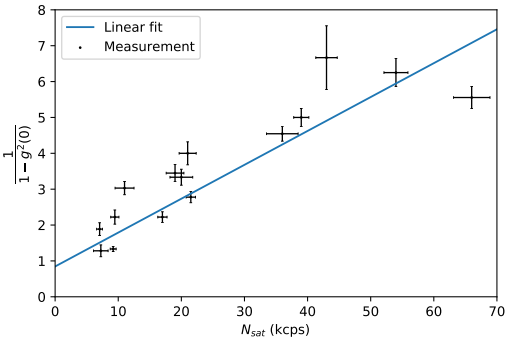

Figure 4.6: *Plot of the estimated amount of NV centers in a nanodiamond vs their brightness.*

4.2 Polarization selective measurements

Single NV center

A 2D polarization plot of a NV center is shown in figure 4.7, where the $x-$ axis represents the polarization angle of the detected light, the $y-$ axis that of the excitation laser and the colour the measured count rate at the photon detector.

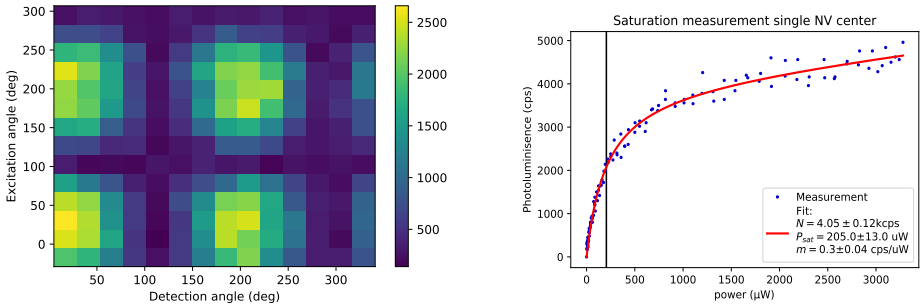

(a) (b)

Figure 4.7: *(a) 2D polarization scan of a single NV center in a nanodiamond. Measurement performed at 350 uW laser power. (b) Saturation measurement* $\alpha_{ex} = \alpha_{det}$*=20.*

By projecting the data onto the excitation and detection axes, we obtain the intensity for excitation angles, as if there were no linear polarizer in detection, and the intensity for detection angles, as if the emitter is excited by unpolarized light, respectively. The former provides information on the absorption dipole of the defect, while the latter provides information on its emission dipole. This projection is performed by summation of all elements of a fixed detection or excitation angle and subsequent normalization:

$$I(\alpha) = \frac{2}{n} \sum_{\beta=0}^{n-1} I_{\alpha\beta} \tag{4.1}$$

where $I(\alpha)$ is the count rate as projected on the α-axis, $n = 15$ the number of elements and $I_{\alpha\beta}$ is the measured count rate for polarization angles α and β. The normalization factor $\frac{2}{n}$ is obtained by averaging $(1/n)$ the counts over all angles and comparison of this average with the total in-

tensity of linearly polarized light (factor 2). The resulting projections are shown in figure 4.8 (a,b).

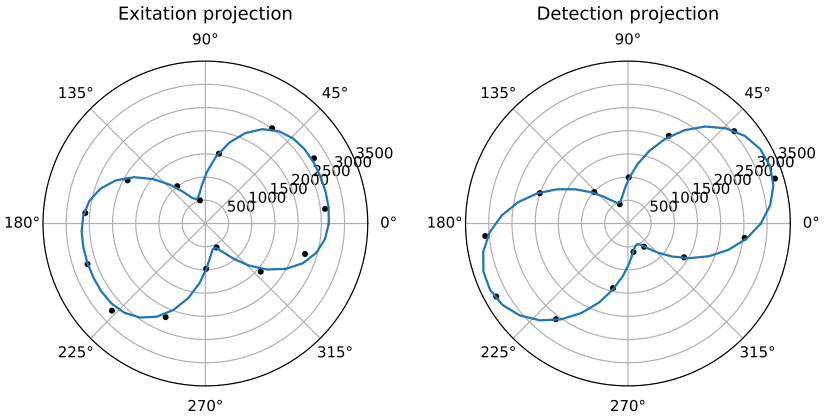

(a) (b)

Figure 4.8: *Projection of count rates from figure 4.7 on the excitation (a) and detection axis (b). Blue curves represent fits of the corresponding equations below.*

The detection projection is fitted to:

$$I_d(\alpha) = mP + B_d + A_d \cos^2(\alpha - \phi_d) \tag{4.2}$$

where m is the background count rate, B_d the offset, A_d the amplitude and ϕ_d the angle of optimal detection. The excitation projection needs a different fit parameter, which is due to the high laser power (350 μW) during the measurement, compared to the saturation power (205 μW). Therefore, for optimal excitation polarization, the NV center is saturated and its intensity does not increase linearly with the excitation power. This effect can be quantified by fit parameter C in the following equation:

$$I_e(\alpha) = mP + B_e + A_e \cos(\alpha - \phi_e)^2(1 - C\cos^2(\alpha - \phi_e)) \tag{4.3}$$

In Appendix B, an elaboration on the origin of equation 4.3 is given and agreement is shown between the *expected value* for C (0.56 ± 0.06), derived from the saturation curve and the laser power, and the *fitted value* for C (0.51 ± 0.03). From the fits of the projections, the polarization contrast in detection is quantified using:

$$C_d = 1 - \frac{I_{d,min} - mP}{I_{d,max} - mP} \tag{4.4}$$

and in excitation with:

$$C_e = 1 - \frac{I_{e,min} - mP}{I_{e,max} - mP} \tag{4.5}$$

giving $P_d = 0.89 \pm 0.005$ and $P_e = 0.83 \pm 0.012$. The optimal angles of detection and excitation are 23.2 ± 0.3 ° and 20.1 ± 0.9 ° respectively.

Two $g^2(\tau)$ measurements of this nanodiamond have been performed for different excitation powers (200 μW and 1000 μW), of which the results are shown in figure 4.9, indicating that the nanodiamond has only one NV center. Note that for these measurements, no background correction is performed and that normalization procedure 2 is performed. As justification for using this procedure, procedure 1 is also performed on the data of 4.9(a) and no deviations were found. In these figures, we observe that the antibunchng timescale is shortened with increasing laser power. Secondly, we observe the emergence of peaks at short time delays.

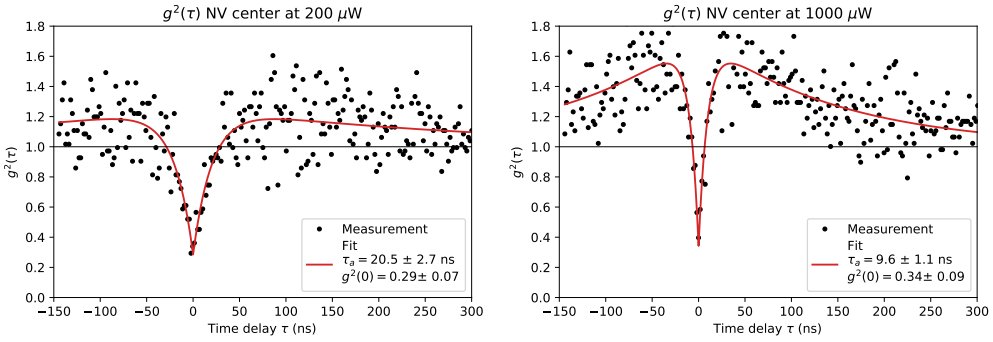

(a) (b)

Figure 4.9: *$g^2(\tau)$ measurement for two excitation powers. The polarization is set equal to that in figure 4.7(b).*

The red curve represents a fit of equation 2.2 to the data. From this fit, we obtain a decrease of the antibunching timescale from 20.5 to 9.6 ns and an increase of the bunching amplitude from 0.25 to 0.75. These effects are predicted by the equations on page 6. An intuitive explanation for the increasing bunchng amplitude is that the third level (dark state) becomes more populated for increasing laser powers. Therefore, by increasing the laser power, the three-level system becomes more clearly visible. We also observe a slight increase in the value for $g^2(0)$ (from 0.29 to 0.34) for increasing laser power. Although theoretically the values for $g^2(0)$ are independent of the excitation power, it is experimentally explainable by the

fact that the background light scales linearly with the excitation power, while the photoluminescence follows the saturation curve. This effect was also found in [18].

Statistics

In total, 18 nanodiamonds have been measured, of which all characteristics can be found in table 4.2. The estimated number of emitters in the nanodiamond, $1/(1-g^2(0))$, is plotted again against the saturation count rate (figure 4.11(a)). From a linear weighted fit, an average brightness per NV center of 3160 $\pm$ 600 cps is found. In figure 4.11(b), a comparison is made between the contrast in detection and in excitation. Here, we observe that for nearly all measured samples, the contrast in detection is higher than in excitation.

Polarization selective NV center results					
Sample	P_{sat} (μW)	N_{sat} (kcps)	$g_2(0)$	τ (ns)	m (cps/μW)
20230503_1	336 $\pm$41	4.3$\pm$0.3	x	x	0.5$\pm$0.08
20230503_2	295 $\pm$ 8	62$\pm$1	x	x	5.6$\pm$0.32
20230503_3	205$\pm$13	4.0$\pm$0.1	0.27$\pm$0.07	29$\pm$2	0.25$\pm$0.04
20230504_1	250$\pm$10	11.1$\pm$0.2	0.78$\pm$0.03	23$\pm$2	1.3$\pm$0.6
20230504_2	447$\pm$32	20$\pm$1	x	x	0.2$\pm$0.2
20230504_3	402$\pm$32	7.9$\pm$0.4	0.77$\pm$0.05	76$\pm$20	0.9$\pm$0.1
20230504_4	301$\pm$15	11.0$\pm$0.3	x	x	0.5$\pm$0.12
20230508_1	884$\pm$0	8.5$\pm$0.3	x	x	0.40$\pm$0.2
20230508_4	550$\pm$32	8.8$\pm$0.5	0.66$\pm$ 0.12	40 $\pm$ 16	0.40$\pm$0.14
20230508_6	302$\pm$26	7.0$\pm$0.4	0.77$\pm$0.08	28$\pm$3	1.7$\pm$0.20
20230509_5	357$\pm$25	15$\pm$0.6	0.76$\pm$0.03	28$\pm$3	1.3$\pm$0.20
20230509_10	790$\pm$40	37$\pm$2	1	x	0.77$\pm$0.43
20230509_20	266$\pm$15	59$\pm$2	1	x	12$\pm$0.90
20230509_50	615$\pm$19	12$\pm$3	x	x	9$\pm$0.71
20230509_100	580$\pm$16	280$\pm$6	x	x	28$\pm$1.6
20230509_gp	306$\pm$12	34$\pm$1	0.91$\pm$0.03	30$\pm$2	2.2$\pm$2.3
20230508_5	370$\pm$23	11$\pm$.04	x	x	1.3$\pm$0.15

Table 4.2: *All measured nanodiamonds in the polarization selective setup.*

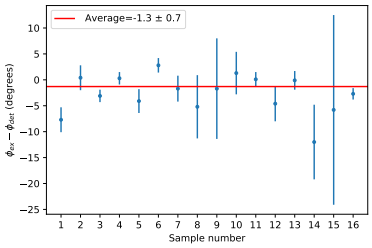

Figure 4.10: *Phase difference between excitation and detection for the samples (in the same order as) shown in table 4.2. Red line is a weighted fit.*

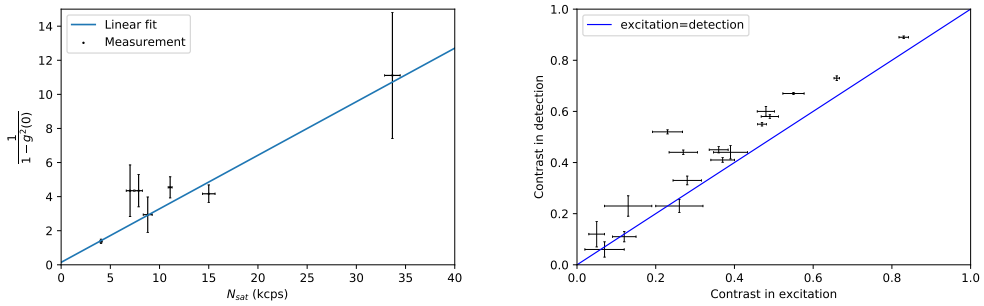

(a) (b)

Figure 4.11: *(a) Number of NV centers in nanodiamonds vs their brightness and (b) a plot of the contrast in detection vs in excitation.*

In figures 4.12(a) and 4.12(b), the contrast in polarization in detection and excitation are plotted against N_{sat} and P_{sat}, respectively. In the former, we observe a decline in contrast for increasing brightness. This is to be expected as the brightness is an indicator of the number of emitters in the sample, which can have different orientations with respect to each other. We also observe, two 'special' nanodiamonds, which are indicated by the green and red circles. The former has a relatively low N_{sat}, while the contrast is low (0.05 in excitation and 0.12 in detection). The latter has a relatively high contrast (0.66 in excitation and 0.73 in detection), while having a high brightness.

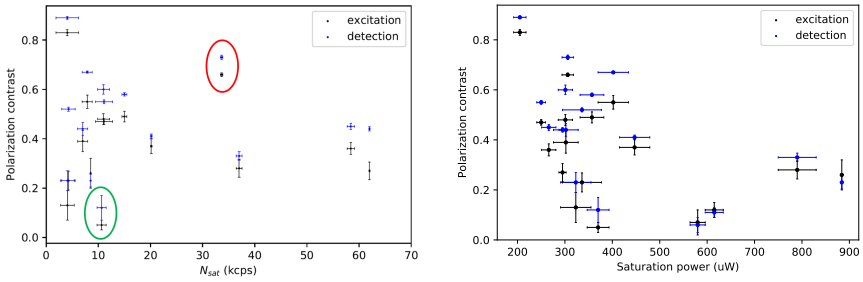

(a) (b)

Figure 4.12: *Polarization contrast vs (a) brightness and (b) saturation power.*

We also observe a decrease in contrast for increasing saturation powers. This might be explained by the fact that P_{sat} of bright nanodiamonds is an average over all excited NV centers in the nanodiamond. If there are many

NV's in different orientations, some are excited more effectively than others and the measured P_{sat} is the average over all centers and is thus an indication of the number of emitters. Hence, if P_{sat} is increased, the number of NV's is higher, resulting in a lower polarization contrast. It has to be noted that this analysis only explains this effect for bright nanodiamonds and not for single NV centers, which is the case for this figure, as only one nanodiamond with a single NV center was found.

The average saturation power of all samples is 421 uW (lowest measured: 205 uW, highest: 890 μW), the average antibunching time scale is 23.8 ns (lowest: 10 ns, highest: 40 ns) and the average phase difference between optimal detection and excitation polarization, $\phi_e - \phi_d$, is -1.3$\pm$0.7° (see figure 4.10 for weighted fit).

Special nanodiamonds

Te 2D polarization scan and projections of the first 'special' nanodiamond, indicated by the green circle in figure 4.12(a) are shown in figure 4.13. Here, we observe four extra regions of high luminescence (compared to figure 4.7(a)), possibly indicating two NV centers, oriented 90° w.r.t. each other. The fits to the projection data are both performed with equation 4.2, as fitting parameter C is only physical if the excitation contrast is high. The higher count numbers for detection angles between 0 and 180° can be explained by the fact that the laserpower was not constant during the measurement.

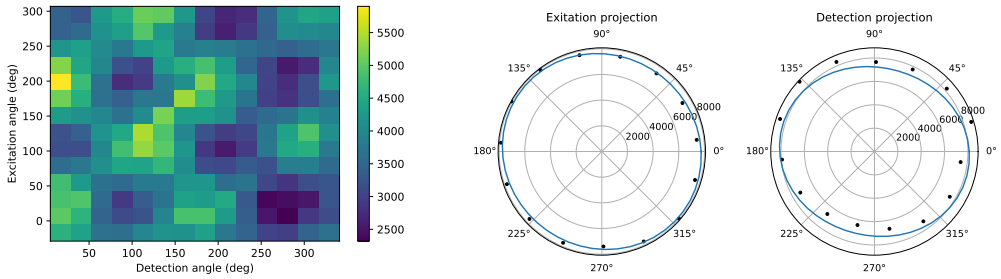

Figure 4.13: *Polarization measurements of the sample indicated by the green circle in 4.12(a).*

In figure 4.14, similar plots are shown for the sample indicated by the red circle. Here we observe a relatively high contrast in both excitation

and detection. This is unusual, as this implies that from the 8 to 14[†] (from a $g^2(\tau)$ measurement) NV centers in the nanodiamond, most are aligned in the same orientation.

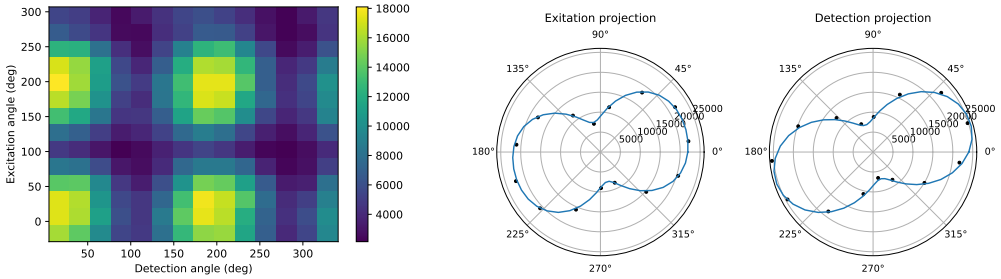

(a) (b) (c)

Figure 4.14: *Polarization measurements of the sample indicated by the red circle in 4.12(a).*

Besides two special nanodiamonds, a very bright (0.6 Mcps) spot of nanodiamonds has been measured, of which the polarization selective measurements are shown in figure 4.15. Here we observe nearly no polarization dependence in excitation and detection. This is to be expected as a large number of nanodiamonds are excited simultaneously, and the dipole orientations of individual NV centers cancel out. The yellow lines indicate equal excitation and detection.

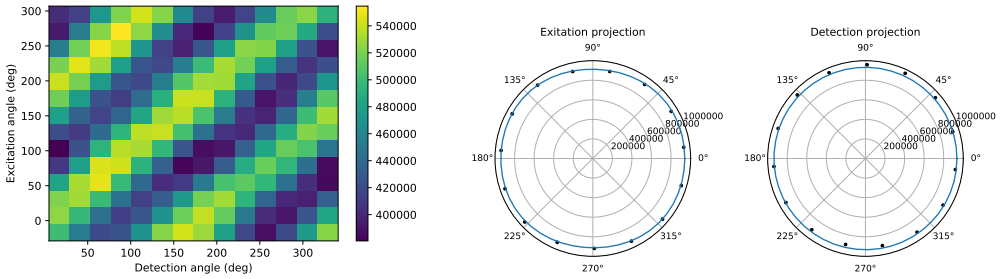

(a) (b) (c)

Figure 4.15: *Polarization measurement of a large number of clustered NDs.*

[†]The closer $g^2(0)$ is to 1, the higher the error in the number of defects.

Version of July 10, 2023– Created July 10, 2023 - 11:45

4.3 Discussion

Polarization selective measurements

From the 2D polarization measurements, the absorption and emission dipole of NV centers in nanodiamonds could be extracted and we found that they have roughly the same orientation (-1.3$\pm$0.7°), which is within the error of the angles of the $\lambda/2$ plate and linear polarizer. The polarization contrast in excitation of a single NV center (0.79 without background correction) is relatively good in comparison to other values in literature: in [19], 0.74 and 0.66 were found for two single NV centers in nanodiamond.

We find that nearly all measured samples have a higher contrast in detection than in excitation. There are (at least) two reasons for this result. (1) the saturation effect, quantified by fit parameter C in equation 4.3, leads to a decrease in the maximum intensity in the excitation projection and thus is C_e decreased. As the detection projection is not influenced by this effect, C_d is not altered. (2) the excitation polarization is not perfectly linear: there can be up to around 1% of the total power in the orthogonal polarization. This results, especially if the laser power is higher than the saturation power, in a lower contrast.

In order to improve on the results in this section, the polarization measurement should be performed well below saturation power, such that introduction of fit parameter C is not necessary, and the polarization contrast in excitation is increased. Also, as only one single NV was found in the polarization selective measurements, more measurements of single NV's would improve the statistical analysis. If this is done, an interesting further investigation would be to obtain statistics on the angle θ of the dipole with the z-axis, which can be obtained from the contrast in excitation using the simple formula [20]:

$$\theta = \cos^{-1}\left(\sqrt{\frac{I_{min}}{I_{max}}}\right) = \cos^{-1}\left(\sqrt{1 - C_e}\right) \tag{4.6}$$

which is verified using ODMR measurements. This formula also allows us to calculate θ for our single NV, giving $\theta = 68 \pm 1°$. A further interesting analysis would be to plot the saturation power vs θ, to find out if the saturation power is a measure of θ. It has to be noted that this formula is only exact for radially polarized beams and is less accurate linear polarized beams, especially for high values of θ. Nevertheless, for values below 50°, small deviations between polarization modes are found [20].

Version of July 10, 2023– Created July 10, 2023 - 11:45

Saturation, brightness, purity and lifetime

The saturation power (205 μW) for our single NV compares well to values in literature: in [21], saturation powers of 662 and 586 μW are found. Our brightness (N_{sat}= 4 kcps), however, is very low compared to these measurements: 52 kcps and 57 kcps, respectively. What limits our brightness compared to [21] is that we only detect 50% of the light, as only 1 detector is used and that our NA is lower (0.9 vs 1.4). In terms of photon purity, our value ($g^2(\tau)$ =0.27 $\pm$ 0.07) is comparable to what is measured in [21], where they found values of 0.24 and 0.41. The average exited state lifetime of 23 ns (where the lowest value is 10 ns and the highest 40 ns) agrees with the findings in [22], where lifetimes between 10 and 40 ns have been reported, with an average of 22 ns for excitation at 530 nm.

Comparison results section 4.1 and 4.2

The advantage of the polarization selective measurement is that we can excite the NV centers more effectively in their dipole orientation. As a result, we are able to obtain lower average saturation powers: 421 vs 660 μW and lower average antibunching time scales 23.8 vs 32.4 ns. The brightness per NV center, obtained from figures 4.6 and 4.11(a), is, however, lower for the polarization selective measurements (3.2 vs 11 kcps). This can be explained by the linear polarizer in detection reflecting a portion of the light and it selecting only one orientation. The latter is more severe for bright nanodiamonds, as for a fixed excitation polarization, the minimum in detection is far from zero (see figure 4.14(a)). As a result, bright nanodiamonds in the polarization selective setup have significantly lower count rates, compared to if they were measured without a linear polarizer in detection. Comparing the $g^2(\tau)$ measurements of single emitters is difficult, as only one single NV in the polarization measurements was found. Nevertheless, we find for this single NV $g^2(0) = 0.27$ without background correction, while of the three NVs in the other setup, without background correction, only one sample has a $g^2(0)$ below zero: $g^2(0) = 0.40$. This can explained by the background being reduced with 50%[‡], while the signal is reduced less.

The polarization selective measurements provide us also with important information on the emitters present in the nanodiamond. Here follows an example to illustrate this importance. It is possible to measure a $g^2(0) < 0.5$ for nanodiamonds with two NVs where one is less bright

[‡]Given that background light is unpolarized.

Version of July 10, 2023– Created July 10, 2023 - 11:45

than the other [23]. This difference in brightness can be a result of the two NVs having a different dipole orientation, similar to in figure 4.14. Therefore, if the information of the polarization is not present, one cannot argue to have sufficient evidence that there is only one emitter in the nanodiamond. Therefore, besides a $g^2(\tau)$ measurement, a polarization selective measurement is needed to provide ultimate proof.

Chapter 5

hBN defect microscopy

The hBN flakes measured in this project are fabricated by colleagues Moritz Fischer and Nicolas Leitherer-Strenger from the Technical University of Denmark. Three defects on the same flake are measured, of which the results are shown subsequently in this chapter.

5.1 Measurements on three defects

Defect 1

In figure 5.1, the $xy-$ scan (a) and saturation measurement (b) of the first hBN defect are shown. As the fitted saturation power could no be reached with the setup, the estimate for m could not be extracted accurately. Therefore, $m = 0.3$ cps/ μW was first obtained from dark spot saturation measurements, after which rough estimates for P_{sat} and N_{sat} are obtained by fitting to equation 2.1.

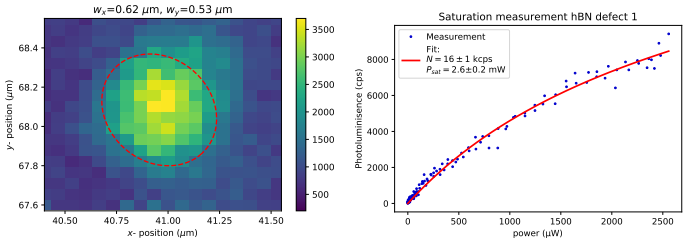

(a) (b)

Figure 5.1: *(a) xy-scan of defect 1, performed at 700 μW and (b) saturation measurement performed at polarization $\alpha_{ex} = \alpha_{det}$=135 °.*

The 2D polarization scan of this defect, including both projections, is shown in figure 5.2. The relatively brighter spot at angles $(\alpha_{ex}, \alpha_{det}) = (330°, 150°)$ is explained by fluctuating laser power. A polarization contrast of 0.76 $\pm$0.02 in excitation and 0.87 $\pm$ 0.01 in detection was found. For fit parameter C, a value of 0.40 $\pm$ 0.04 was extracted, which is in agreement with the expected value, 0.38 $\pm$ 0.05 (see Appendix B). The phase difference between excitation and detection, $\phi_{ex} - \phi_{det}$, is measured to be -7 $\pm$ 1°.

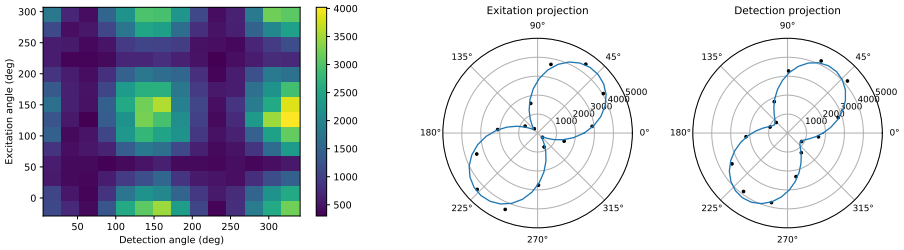

(a) (b) (c)

Figure 5.2: *Polarization measurements of hBN defect 1 at 700-850 μW laser power.*

A $g^2(\tau)$ measurement of this defect can be found in figure 5.3. Here, normalization method 2 of section 3.3 could not be performed as $g^2(\tau)$ is not constant at long timescales (see figure (b)), and hence method 1 is applied. Unfortunately, due to a drift in the setup and a fluctuating laser power (500-700 μW), the measured count rate is not constant. As only the count rate at the beginning (2.9 kcps) and end (2.3 kcps) of the experiment are known, the average of the two is used as count rate in the normalization in equation 3.3 As a result, the values of $g^2(\tau)$ represent an upper bound.

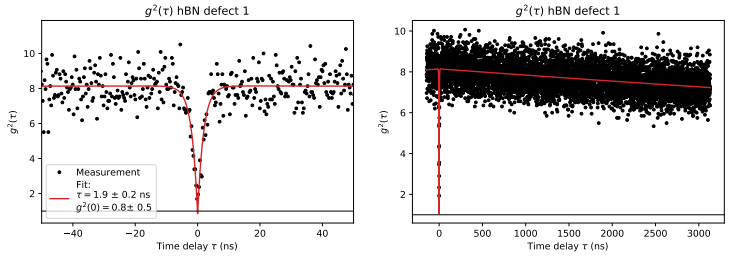

(a) (b)

Figure 5.3: *$g^2(\tau)$ for (a) short and (b) long time scales (same measurment). Performed at 500-700 μW laser power.*

A spectrum of this defect is shown in figure 5.4(a), where we observe emission between 2.0 and 2.2 eV (560-620 nm) and a clear peak around 2.16 eV (574 nm). We also observe a smaller peak around 2.05 eV.

The origin the clear peak is the Raman shift, Δv [m^{-1}], which is calculated by:

$$\Delta v = \frac{1}{\lambda_0} - \frac{1}{\lambda_1} \tag{5.1}$$

where λ_0 is the excitation wavelength (532 nm) and λ_1 the wavelength of the Raman peak (574 nm), giving a Raman shift of 1375 cm^{-1}. This value is similar to findings in [24], where a Raman shift of 1367 cm $^{-1}$ is measured using a 514 nm excitation laser.

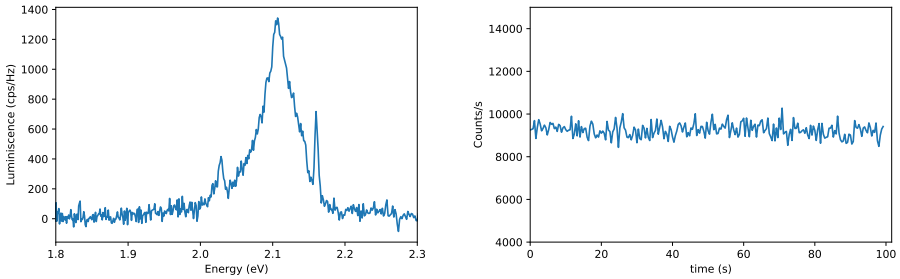

(a) (b)

Figure 5.4: *(a) Spectrum (b) and time trace measurement of defect 1. Both measurements performed at 900 μW.*

A time trace measurement over 100 seconds can be found in figure 5.4(b), where we observe a relatively constant photoluminescence. Note that in this measurement, both detectors are turned on, and the measured count rate is the sum of the count rates at both detectors. This explains the high count rates compared to figure 5.1(b).

Defect 2

A saturation measurement of this defect can be found in figure 5.5. We again observe that the laser power is not high enough to reach saturation and that our values for P_{sat} and N_{sat} have therefore a large error (P_{sat} = 3.3 $\pm$ 0.7 mW, N_{sat} = 35 $\pm$ 10 kcps).

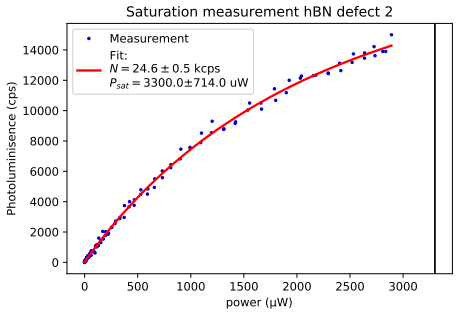

Figure 5.5: *Saturation measurement of defect 2 performed at polarization (α_{ex}, α_{det})=(50°,50°).*

The 2D polarization scan is shown in figure 5.6, from which we obtain a polarization contrast in excitation of 0.97 $\pm$ 0.02 and in detection of 0.83 $\pm$ 0.2*. The value for fit parameter C of the saturation effect is found to be 0.19 $\pm$ 0.09, where the expected value is (Appendix B) 0.20 $\pm$ 0.05. We find that $\phi_{ex} - \phi_{det}$ = -9 $\pm$ 2.

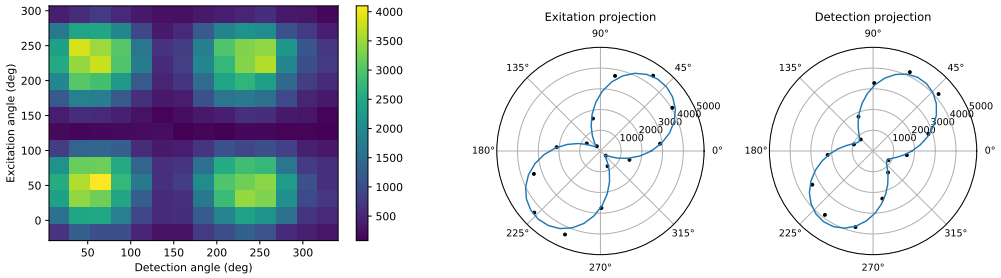

(a) (b) (c)

Figure 5.6: *2D polarization measurement of hBN defect 2, performed at 500 µW.*

In figure 5.7, a $g^2(\tau)$ measurement of this defect is shown, where the same normalization method is performed as for the previous sample. Due

*Without background correction, C_e =0.93 $\pm$ 0.02.and C_d = 0.80 $\pm$ 0.02.

to a higher laser power than for defect 1 (1000 vs 500 μW), we obtain a a higher count rate and the duration of the measurement could be shortened. This results in a smaller decrease (from 9 to 7 kcps) of the count rate over time and the result is thus more reliable than that of defect 1. We find a $g^2(\tau)$ of 0.09 $\pm$ 0.06, clearly indicating that the defect is a single photon source. In figure (b), we observe that $g^2(\tau)$ is not yet constant at 3000 ns, similar to figure 5.3.

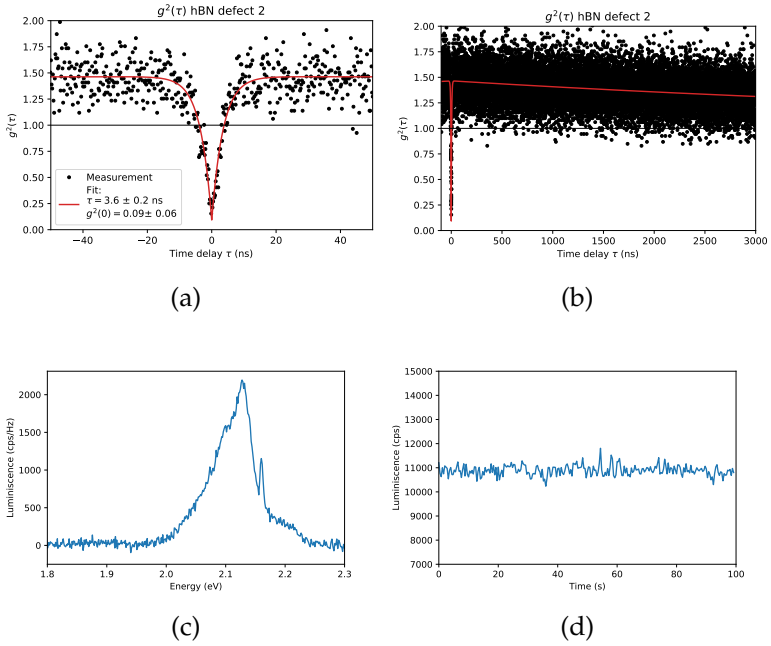

Figure 5.7: *$g^2(\tau)$ for (a) short and (b) long time scales (same measurement, performed at 1000 μW). (c) spectrum (at 400 μW) and (d) time trace (at 600 μW).*

The spectrum is shown in figure 5.7(c), where we observe again a similar Raman wavelength and emission between 2.0 and 2.2 eV. In figure 5.7(d), we observe a constant photoluminescence over 100 s.

Version of July 10, 2023– Created July 10, 2023 - 11:45

Defect 3

This defect showed quite different behaviour from the previous two defects, especially in saturation and polarization. The saturation curve is shown in figure 5.8(a). This curve shows clear saturation with a relatively low P_{sat} (0.22 $\pm$ 0.01 mW) and N_{sat} (3.2 $\pm$ 0.5 kcps). In polarization (figures 5.8(b-d)), we observe the following in the excitation projection: (1) the measured count rate is asymmetric around its maxima and (2) the luminisence is relatively constant, except around 70° and 250°, showing clear dips. In detection, a usual plot is obtained, where C_e =0.94$\pm$ 0.02 [†]is found from the fit. Interestingly, the angle of optimal excitation (225°) and detection (163°) deviate significantly, although it has to be noted that the accuracy of the optimum excitation angle is low.

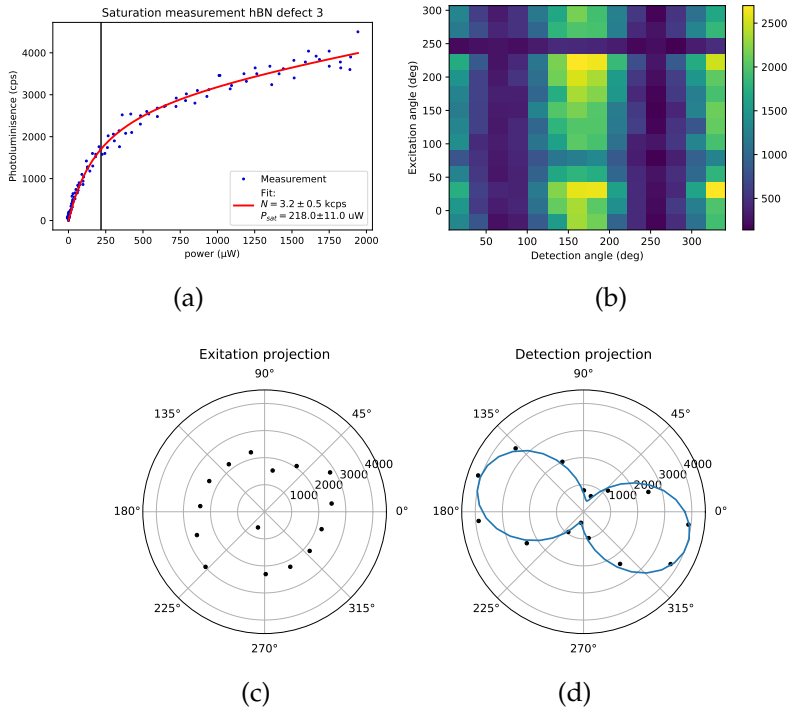

Figure 5.8: *(a) Saturation measurement (at polarization: $\alpha_{det} = 163$, $\alpha_{ex} = 225$), (b) 2D polarization scan (performed at 600 μW), (c) and (d) excitation and detection projections, respectively.*

A partial explanation of the relatively flat excitation projection is that the

[†]Without background correction, C_d =0.90$\pm$ 0.02.

polarization measurement is performed at 3 times the saturation power. The origin of the asymmetry around the maximum intensity, however, cannot be explained by this effect and remains unknown.

The $g^2(\tau)$ measurement is shown in figure 5.9. As the brightness of this defect is relatively low, the measurement duration was long and therefore, the decrease of the count rate is high (from 2.2 to 1.1 kcps). As a result, the normalization is not very reliable and $g^2(\tau)$ represents an upper bound. We obtain $g^2(0) = 0.4 \pm 0.3$. Due to the large error, we cannot ultimately decide whether this defect is a single photon source. Over long time scales, we observe a steep decrease of $g^2(\tau)$ (from 4.2 to 2.7).

The spectrum of the defect is shown in 5.9(c), where the Raman peak is relatively high, as the brightness of the emitter is relatively low compared to the background, which is the source of the Raman shift. The range of emission (1.9-2.3 eV) is relatively wide compared to the previous defects, and a second peak is found at 2.25 eV.

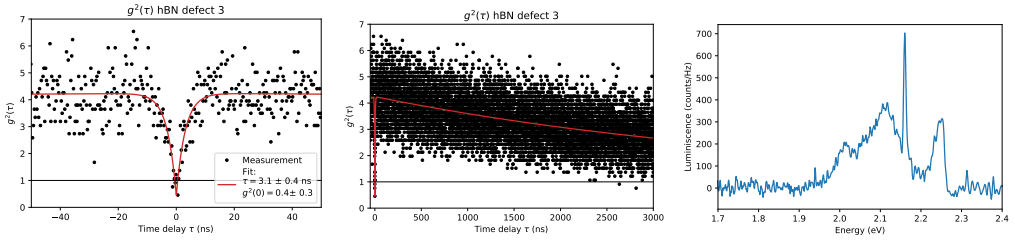

(a) (b) (c)

Figure 5.9: *$g^2(\tau)$ for (a) short and (b) long time scales (same measurement, performed at 380 μW). (c) spectrum.*

Polarization selective hBN results					
Sample	P_{sat} (mW)	N_{sat} (kcps)	$g_2(0)$	$g_2(3000\text{ ns})$	τ (ns)
defect 1	2.6 $\pm$0.2	16$\pm$1	0.8$\pm$0.5	7.3	1.9$\pm$ 0.2
defect 2	3.3 $\pm$0.7	35$\pm$10	0.09$\pm$0.06	1.3	3.6$\pm$ 0.06
defect 3	0.4 $\pm$0.3	3.2$\pm$0.5	0.8$\pm$0.5	2.7	3.1$\pm$ 0.4

Table 5.1: *All measured hBN defects in the polarization selective setup.*

Version of July 10, 2023– Created July 10, 2023 - 11:45

5.2 Discussion

Defect measurements

Here, the results of the defects are discussed and compared, and improvements on the measurements are proposed. The polarization selective measurements of defects 1 and 2 show that the absorption and emission patterns are similar in shape and orientation, while defect three shows clear deviations. A difference between defects 1 and 2 is that for defect 1, the detection contrast was higher than the excitation contrast, while we found the opposite for defect 2. This cannot be explained fully by the saturation effect. We found similar mismatches between optimal excitation and detection angles ($\Delta\phi_1$= -7 $\pm 1^\circ$, $\Delta\phi_2$ = -9$\pm 2^\circ$), which fall within their margins of error. As the uncertainty of the angles of the HWP and the linear polarizer at that time was around a few degrees, it is not clear whether this mismatch is physical. In order to improve on the polarization measurements, these angles should be measured more accurately and the polarization scan should be performed with lower laser power, to reduce the saturation effect as qauntified by fit parameter C.

For all hBN samples we observe a non-perfect polarization contrast in excitation and in detection. A suggested origin for the non-ideal *excitation* contrast is the angle θ between the dipole and the normal of the $xy-$ plane. The value of this contrast is directly related (see equation 4.6) to θ [20] as long as θ is below 50°. The origin of the high contrast for defect 2 (0.97) compared to defect 1 (0.76) might thus be angle θ. As a multi-layer flake is measured, it is possible that different defects have slightly different orientation w.r.t. the xy-plane. The origin of the non-ideal contrast in *detection* (0.83 and 0.87), however cannot be explained by this effect, and remains unknown. It has to be noted that the measured polarization contrasts here are not unexpected as in [10] similar values (~ 0.8) are reported.

Due to the drift in the optical setup and laser power variations, the normalizations of defects 1 and 3 are not up to standard and values for $g^2(0)$ of these two defects are unreliable. In order to have a better normalization for long measurements, the count rate at the detectors should be saved every second and the average should be used in the normalization. The antibunching timescale is fortunately not affected by this problem, of which we found an average of 2.9 ns.

We found an interesting relation between the relative decay of $g^2(\tau)$ over long timescales and ratio $\frac{P}{P_{sat}}$, where P is the laser power during a $g^2(\tau)$ measurement. For defects 1 and 2, this decay is small (from 8.2 to 7.2 and 1.42 to 1.31 over 3000 ns), as is $\frac{P}{P_{sat}}$ (0.2 and 0.3). For defect 3

Version of July 10, 2023– Created July 10, 2023 - 11:45

however, we find a decay from $g^2(\tau)$ =4.2 to 2.7 at 3000 ns, while $\frac{P}{P_{sat}} = 5$. This suggests that a high value for $\frac{P}{P_{sat}}$ results in a steeper slope of $g^2(\tau)$. This effect has also been studied in [25], where $g^2(\tau)$ measurements have been performed up to 100 μs for varying $\frac{P}{P_{sat}}$, showing similar results. An interesting future experiment is therefore the measurement of $g^2(\tau)$ for a variety of laser powers *on the same defect*.

The spectrum of a defect provides information on the type of defect [15] ($V_N C_B$ or V_B^-), as discussed in section 2.3. By comparing our spectra to the typical spectra of the two types (see figure 2.7), we speculate that defects 1 and 2 are of type 2, as only one peak is visible and that defect 3 is of type 1, as two peaks are visible. The similarities between what is found in literature and our results are not very clear, so the above statement is a mere hypothesis that needs further investigation.

Comparison defect 2 and literature

As defect 2 showed the best results, we compare here the important measured quantities of this defect to other values for hBN defects found in literature. Our result of $g^2(0)$ =0.09$\pm$ 0.06 compares well with with 0.25 in [26] and 0.069 $\pm$ 0.403 in [15]. Concerning polarization measurements, our contrasts (without background correction) in excitation (0.93 $\pm$ 0.02) and detection (0.80 $\pm$ 0.02) are similar to the results of multilayer hBN flakes in [26](estimated from figure 3), where an excitation contrast of 0.93 and detection contrast of 0.84 were measured. In terms of brightness, similar to the NV center measurements, we measure a fairly low intensity (N_{sat} = 35 kcps), where in [26] count rates in the order of MHz are reported. The measured saturation power (3.3 mW) is relatively high compared to values found in [26], where a saturation power of 611 μW was measured.

Version of July 10, 2023– Created July 10, 2023 - 11:45

Chapter 6

Concluding summary and outlook

This chapter compares the results of NV centers in nanodiamond and hBN defects, and summarizes the general findings of this project. It ends with a brief outlook for future experiments.

We found that hBN defect 2 ($g^2(0) = 0.09 \pm 0.06$) showed a higher single photon purity compared to the best NV center ($g^2(0) = 0.29 \pm 0.07$), without background correction. Poisonian statistics ($g^2(\tau)$ =1) are reached around 600 ns for nanodiamonds, while for hBN, $g^2(\tau)$ did not reach 1 even at 3000 ns for all defects. For the hBN defects, a lower average antibunching time scale is measured (2.9 ns) than for NV centers (23 ns). The polarization contrasts indicate that the absorption dipole of hBN (0.97) is sharper than for the NV center (0.83), while the emission dipoles are similar (0.83 vs 0.87). This might be explained by the hBN defects orientation being parallel with the $xy-$ plane, while the NV centers' orientation w.r.t. the xy-plane are randomly distributed. In saturation measurements, clear differences were found: for the single NV we found $P_{sat} = 200$ μW and $N_{sat} = 4$ kcp, while for hBN defect 2 we found $P_{sat} = 3300$ μW and $N_{sat} = 35$ kcps, although with higher inaccuracy. This difference might be explained by the higher antibunching time scale of NV centers, limiting the emitters brightness and decreasing the saturation power. In terms of spectral properties, we found a narrower emission spectrum for hBN (560-620 nm), compared to the NV centers (600-780 nm). So for the crucial SPS parameters of purity, brightness, and polarization contrast, better results were obtained for the hBN defect.

Generally, we found that we can excite SPSs more efficiently by including polarization selective elements in the optical setup, as the saturation power could be significantly decreased compared to the non polarization selective measurement for NVs. Another benefit of polarization measure-

ments is that we obtain information on the emitters absorption and emission dipoles, which, as discussed in section 4.3, is crucial to state whether we measure a true single photon source. Also, the background is reduced compared to the luminescence of the SPS, resulting in a lower $g^2(0)$.

The results presented in this thesis can be improved by two simple adjustments. The first is performing the polarization measurements at laser powers well below saturation. The second is that in order to accurately determine $g^2(\tau)$ for hBN defects, the count rate should be known over the course of the measurement.

An interesting future experiment is the measurement of the bunching effect for hBN defects for a variety of laser powers. This experiment might be difficult as for high laser powers, defects can bleach fast. Such experiments might provide us with information on the level system of hBN defects, similarly to what is found for the NV centers. Secondly, more flakes need to be measured, as the defects in this thesis are all located on the same flake. As flakes can have a variety of thicknesses, the defects might exhibit strong deviations in their photoluminescent behaviour, possibly giving better results.

Version of July 10, 2023– Created July 10, 2023 - 11:45

Appendix A

Correcting the polarization dependent reflection amplitude of the dichroic mirror

Here, the procedure to correct for the polarization dependent reflection amplitude of the dichroic is shown. First of all, let us illustrate the problem: upon rotating the polarization of the excitation laser, we measure an oscillating power before the objective, as shown in figure A.1. It has to be noted that this figure is without the inclusion of the birefringent crystal in the optical setup. Nevertheless, the qualitative behaviour is similar, as only the oscillation amplitude is significantly smaller after inclusion of this element.

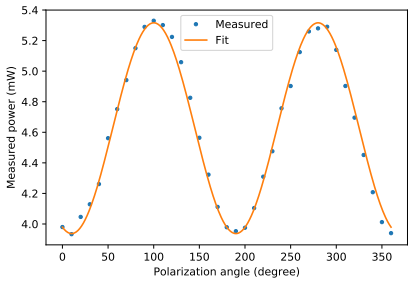

Figure A.1: *Power measurement for different polarization angles of excitation.*

By fitting the data to a $B + A\cos^2(\alpha - \phi)$ function, we get:

$$P = 3.94 + 1.38\cos^2(\alpha - \phi) \tag{A.1}$$

where α is the polarization angle and $\phi = 100\ ^\circ$. We have thus a power modulation of 1.38 mW, on top of a base power of 3.94 mW.

The idea is then to modulate the laser power with the attenuator such that P is flat and has value 3.94 mW. In order to do this, the relation between the attenuator voltage V and the resulting power needs to be extracted, which is done by measuring the laser power for different attenuator voltages (see figure A.2) and fitting to a Lorentzian to the power 4, giving:

$$P = 4.04\left(\frac{\gamma^2}{V^2+\gamma^2}\right)^4 \tag{A.2}$$

where $\gamma = 1.1$.

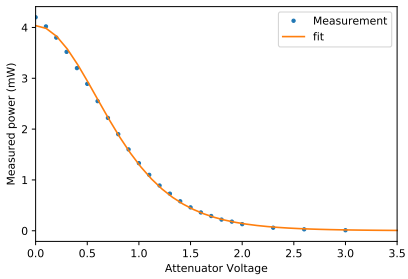

Figure A.2: *Power measurement for attenuator voltages.*

Now, given that we are performing a polarization measurement at V, we need to find the change in voltage ΔV such that the laser power is decreased a factor 5.32/3.94=1.35. This value can be quantified by solving:

$$\frac{\left(\frac{\gamma^2}{\gamma^2+V^2}\right)^4}{\left(\frac{\gamma^2}{\gamma^2+(V+\Delta V)^2}\right)^4} = 1.35 \tag{A.3}$$

which can be simplified by using that $(\Delta V)^2 = 0$. This gives then the following equation for ΔV:

$$\Delta V = \frac{0.078(\gamma^2+V^2)}{2V} \tag{A.4}$$

which is tweaked a bit further using trial and error to obtain a constant fraction $\frac{P_V}{P_{V+\Delta V}}$ for attenator voltages between 1 and 2.5 V, which is the typ-

ical operating region during polarization selective measurements. This results in the following expression for ΔV:

$$\Delta V = \frac{0.075(\gamma^2 + (V + 0.08)^2)}{2(V + 0.08)} \tag{A.5}$$

of which the resulting laser power fractions for the interesting attenuator voltages are shown in figure A.3 indicating a stable power reduction of factor 1.35.

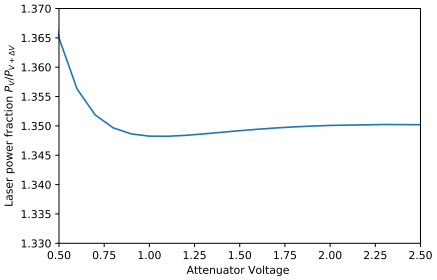

Figure A.3: *Estimated laser power reduction factors for different attenutor voltages.*

Finally, we need to adjust the attenuator voltage every time the polarization is varied. In order to do this, we simply use the shape of equation A.2 and fill in the important parameters, given that we perform the measurement at attenuator voltage V_0:

$$V(\alpha) = V_0 + \Delta V \cos^2(\alpha - \phi) \tag{A.6}$$

where $\alpha = 100°$ and ΔV is given by equation A.5. This formula is incorporated in the Python script for polarization selective measurements. Upon measuring the power during such a measurement with the power correction turned on, deviations from a constant power of maximally 1 % were found.

Appendix B

Polarization dependent saturation correction

In this appendix, an elaboration is given on the introduction of fit parameter C in equation 4.3, and the physical origin of the fitted value is related to a saturation measurement.

The shape of the saturation effect, a multiplication of equation 4.2 by factor $(1 - C\cos^2(\alpha_e - \phi_e))$, is an Ansatz that must fulfill the following assumptions:

1. The saturation power increases with the polarization mismatch of the excitation laser and the absorption dipole.
2. The saturation effect is maximal for zero polarization mismatch. This means that where the brightness reaches its maximum, it is also maximally 'damped' by the saturation effect. This is the case, as the ratio $\frac{P}{P_{sat}}$ is maximal (P is the constant excitation laser power).
3. The saturation effect is minimal for maximal polarization mismatch, as ratio $\frac{P}{P_{sat}}$ is minimal.

Upon inspection, it is clear that multiplication by the aforementioned factor satisfies the above constraints and it fits the data almost perfectly. However, a direct mathematical derivation is omitted here. Therefore, the shape of the saturation effect remains an Ansatz. In order to obtain a more physically intuitive equation, factor $P/P_{sat}(\alpha)$ should be included, where $P_{sat}(\alpha)$ is the excitation polarization dependent saturation power. However, as this saturation effect is a mere artifact of the performance of the polarization measurement at too high laserpowers, which can easily be avoided, this inclusion is omitted in this thesis.

In order to test whether the fitted value of C is physical, we calculate the expected count rate at optimal polarization if $\frac{P}{P_{sat}}$ is small, such that a saturation measurement shows linear behaviour. We can then compare this count rate I_{exp} with the measured count rate I_{meas} to obtain an estimate for fit parameter C, independently of the polarization measurements. We calculate this value from the saturation curve at optimal detection and excitation polarization, as shown in figure 4.7(b). In order to find I_{exp}, we use the derivative of the saturation curve w.r.t the excitation power(see 2.1) at $P = 0$:

$$\left.\frac{\partial I}{\partial P}\right|_{P=0} = \frac{N_{sat}}{P_{sat}} \tag{B.1}$$

With this value, we can calculate $I_{exp}(P) = \frac{Nsat}{P_{sat}}P$, which represents the NV's brightness, if there was no saturation effect. In figure B.1, the saturation measurement is shown again with inclusion of $I_{exp}(P)$.

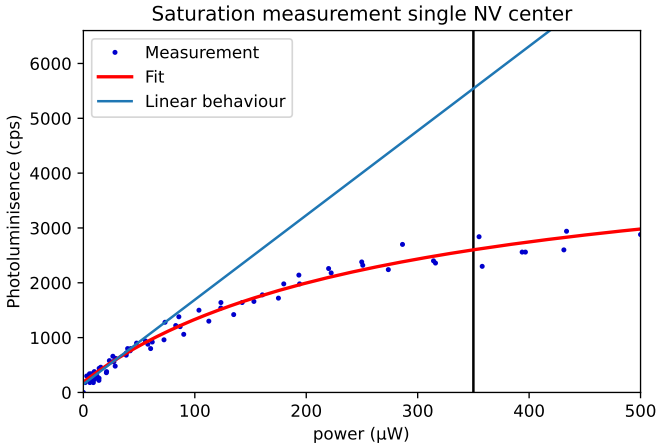

Figure B.1: *Saturation curve with inclusion of $I_{exp}(P)$, where the vertical line indicates the laser power of the 2D polarization measurement.*

Now, we can relate the ratio $\frac{I_{meas}}{I_{exp}}$, which simply is the ratio between the red and blue curve at 350 μW, to the expected value for fit parameter C:

$$C_{exp} = 1 - \frac{I_{meas}}{I_{exp}} \tag{B.2}$$

which gives $C = 0.56 \pm 0.06$. Similar calculations have been performed for hBN defects 1 and 2.

Version of July 10, 2023– Created July 10, 2023 - 11:45

Bibliography

[1] M. W. Doherty, N. B. Manson, P. Delaney, F. Jelezko, J. Wrachtrup, and L. C. Hollenberg, "The nitrogen-vacancy colour centre in diamond," *Physics Reports*, vol. 528, no. 1, pp. 1–45, 2013.

[2] X. He, H. Htoon, S. K. Doorn, W. H. Pernice, F. Pyatkov, R. Krupke, A. Jeantet, Y. Chassagneux, and C. Voisin, "Carbon nanotubes as emerging quantum-light sources," *Nature Materials*, vol. 17, no. 8, pp. 663–670, 2018.

[3] F. P. García de Arquer, D. V. Talapin, V. I. Klimov, Y. Arakawa, M. Bayer, and E. H. Sargent, "Semiconductor quantum dots: Technological progress and future challenges," *Science (New York, N.Y.)*, vol. 373, no. 6555, 2021.

[4] S. Castelletto, F. A. Inam, S. I. Sato, and A. Boretti, "Hexagonal boron nitride: A review of the emerging material platform for single-photon sources and the spin-photon interface," *Beilstein Journal of Nanotechnology*, vol. 11, pp. 740–769, 2020.

[5] I. Aharonovich, D. Englund, and M. Toth, "Solid-state single-photon emitters," *Nature Photonics*, vol. 10, no. 10, pp. 631–641, 2016.

[6] W. Pfaff, B. J. Hensen, H. Bernien, S. B. Van Dam, M. S. Blok, T. H. Taminiau, M. J. Tiggelman, R. N. Schouten, M. Markham, D. J. Twitchen, and R. Hanson, "Unconditional quantum teleportation between distant solid-state quantum bits," *Science*, vol. 345, no. 6196, pp. 532–535, 2014.

[7] B. Hensen, H. Bernien, A. E. Dreaú, A. Reiserer, N. Kalb, M. S. Blok, J. Ruitenberg, R. F. Vermeulen, R. N. Schouten, C. Abellán, W. Amaya,

V. Pruneri, M. W. Mitchell, M. Markham, D. J. Twitchen, D. Elkouss, S. Wehner, T. H. Taminiau, and R. Hanson, "Loophole-free Bell inequality violation using electron spins separated by 1.3 kilometres," *Nature*, vol. 526, no. 7575, pp. 682–686, 2015.

[8] R. Schirhagl, K. Chang, M. Loretz, and C. L. Degen, "Nitrogen-vacancy centers in diamond: Nanoscale sensors for physics and biology," *Annual Review of Physical Chemistry*, vol. 65, pp. 83–105, 2014.

[9] S. W. Jeon, J. Lee, H. Jung, S. W. Han, Y. W. Cho, Y. S. Kim, H. T. Lim, Y. Kim, M. Niethammer, W. C. Lim, J. Song, S. Onoda, T. Ohshima, R. Reuter, A. Denisenko, J. Wrachtrup, and S. Y. Lee, "Bright Nitrogen-Vacancy Centers in Diamond Inverted Nanocones," *ACS Photonics*, vol. 7, no. 10, pp. 2739–2747, 2020.

[10] N.-J. Guo, Y.-Z. Yang, X.-D. Zeng, S. Yu, Y. Meng, Z.-P. Li, Z.-A. Wang, L.-K. Xie, J.-S. Xu, J.-F. Wang, Q. Li, W. Liu, Y.-T. Wang, J.-S. Tang, C.-F. Li, and G.-C. Guo, "Coherent control of an ultrabright single spin in hexagonal boron nitride at room temperature," 2023.

[11] L. Novotny and B. Hecht, *Principles of Nano-Optics*, vol. 10. Cambridge: Cambridge University Press, second ed., 2007.

[12] S. Ishii, S. Saiki, S. Onoda, Y. Masuyama, H. Abe, and T. Ohshima, "Ensemble Negatively-Charged Nitrogen-Vacancy Centers in Type-Ib Diamond Created by High Fluence Electron Beam Irradiation," *Quantum Beam Science*, vol. 6, mar 2022.

[13] L. Rondin, G. Dantelle, A. Slablab, F. Grosshans, F. Treussart, P. Bergonzo, S. Perruchas, T. Gacoin, M. Chaigneau, H. C. Chang, V. Jacques, and J. F. Roch, "Surface-induced charge state conversion of nitrogen-vacancy defects in nanodiamonds," *Physical Review B - Condensed Matter and Materials Physics*, vol. 82, no. 11, pp. 1–5, 2010.

[14] W. Liu, N.-J. Guo, S. Yu, Y. Meng, Z.-P. Li, Y.-Z. Yang, Z.-A. Wang, X.-D. Zeng, L.-K. Xie, Q. Li, J.-F. Wang, J.-S. Xu, Y.-T. Wang, J.-S. Tang, C.-F. Li, and G.-C. Guo, "Spin-active defects in hexagonal boron nitride," *Materials for Quantum Technology*, vol. 2, p. 032002, sep 2022.

[15] M. Fischer, J. M. Caridad, A. Sajid, S. Ghaderzadeh, M. Ghorbani-Asl, L. Gammelgaard, P. Bøggild, K. S. Thygesen, A. V. Krasheninnikov, S. Xiao, M. Wubs, and N. Stenger, "Controlled generation of luminescent centers in hexagonal boron nitride by irradiation engineering," *Science Advances*, vol. 7, no. 8, 2021.

[16] A. Beveratos, S. Kühn, R. Brouri, T. Gacoin, J. P. Poizat, and P. Grangier, "Room temperature stable single-photon source," *European Physical Journal D*, vol. 18, no. 2, pp. 191–196, 2002.

[17] M. Gu, Y. Cao, S. Castelletto, B. Kouskousis, and X. Li, "Superresolving single nitrogen vacancy centers within single nanodiamonds using a localization microscope," *Optics Express*, vol. 21, no. 15, p. 17639, 2013.

[18] B. Rodiek, M. Lopez, H. Hofer, G. Porrovecchio, M. Smid, X.-L. Chu, S. Gotzinger, V. Sandoghdar, S. Lindner, C. Becher, and S. Kuck, "Experimental realization of an absolute single-photon source based on a single nitrogen vacancy center in a nanodiamond," *Optica*, vol. 4, no. 1, p. 71, 2017.

[19] J. Christinck, B. Rodiek, M. López, H. Hofer, H. Georgieva, and S. Kück, "Characterization of the angular-dependent emission of nitrogen-vacancy centers in nanodiamond," *Applied Physics B: Lasers and Optics*, vol. 126, no. 10, pp. 1–8, 2020.

[20] P. R. Dolan, X. Li, J. Storteboom, and M. Gu, "Complete determination of the orientation of NV centers with radially polarized beams," *Optics Express*, vol. 22, no. 4, p. 4379, 2014.

[21] F. Hirt, J. Christinck, H. Hofer, B. Rodiek, and S. Kück, "Sample fabrication and metrological characterization of single-photon emitters based on nitrogen vacancy centers in nanodiamonds," *Engineering Research Express*, vol. 3, no. 4, 2021.

[22] J. Storteboom, P. Dolan, S. Castelletto, X. Li, and M. Gu, "Lifetime investigation of single nitrogen vacancy centres in nanodiamonds," *Optics Express*, vol. 23, no. 9, p. 11327, 2015.

[23] D. Y. M. Peng, J. G. Worboys, Q. Sun, S. Li, M. Capelli, S. Onoda, T. Ohshima, P. Reineck, B. C. Gibson, and A. D. Greentree, "Quantum polarization mapping of nitrogen-vacancy centers in diamond," 2022.

[24] D. G. Purdie, N. M. Pugno, T. Taniguchi, K. Watanabe, A. C. Ferrari, and A. Lombardo, "Cleaning interfaces in layered materials heterostructures," *Nature Communications*, vol. 9, no. 1, pp. 1–12, 2018.

[25] M. K. Boll, I. P. Radko, A. Huck, and U. L. Andersen, "Photophysics of quantum emitters in hexagonal boron-nitride nano-flakes," *Optics Express*, vol. 28, no. 5, p. 7475, 2020.

[26] T. T. Tran, K. Bray, M. J. Ford, M. Toth, and I. Aharonovich, "Quantum emission from hexagonal boron nitride monolayers," *Nature Nanotechnology*, vol. 11, pp. 37–41, jan 2016.